Konstantinos AKRITIDIS

Micro- and Nano- Technologies for Integrated Systems
2019-2021

IMEP-LaHC - 3, Parvis Louis Néel, Grenoble

Integrated optical circuits and dielectrophoresis: Towards bacterial sensing applications

from 08/02/21 to 31/07/21

Confidentiality: No

Under the supervision of:

- **Supervisors:**
Elise, GHIBAUDO, elise.ghibaudo@grenoble-inp.fr
Davide, BUCCI, davide.bucci@phelma.grenoble-inp.fr

Present at the defense: Yes

- **Phelma Tutor:**
Jean-Emmanuel, BROQUIN, broquin@minatec.grenoble-inp.fr

Ecole nationale
supérieure de physique,
électronique, matériaux

Phelma
Bât. Grenoble INP - Minatec
3 Parvis Louis Néel - CS 50257
F-38016 Grenoble Cedex 01

Tél +33 (0)4 56 52 91 00
Fax +33 (0)4 56 52 91 03

http://phelma.grenoble-inp.fr

Acknowledgements

During this project I had the pleasure of working with several people of various backgrounds. Despite the risk of being deemed unoriginal, I cannot find even one that had not left a positive mark in my mind.

First and foremost, I would like to express my sincere gratitude to my supervisors Elise GHIBAUDO and Davide BUCCI for all their contributions so far. Their deep knowledge and experience were both expected and verified throughout our many interactions. What I was not able to predict beforehand however, was their humility and strong work ethics. They undertook their supervising tasks with extreme care and moreover gave me insights on the life of a researcher, without projecting arrogance in any shape or form.

Next I would like to thank Aude BOUCHARD and Gregory GROSA for training me in various technological processes and for making sure I have everything I needed for my experiments. Their patience and attitude to help were a joy to witness.

I am also thankful to PhD candidates Olfa KARKER and Léo HETIER. Olfa for her immense generosity to share both her knowledge and time with me and Léo for doing a very good job at his master thesis last year, which allowed me to move this project with great momentum.

Finally, I would like to thank my tutor Jean-Emmanuel BROQUIN as well as Dominique RAULY, Xavier MESCOT and Pascal XAVIER for their contributions and the time they so willingly shared with me.

Creating a fair and encouraging environment can only push you towards working on the essence of things. And this is something that the whole team should feel proud for having accomplished.

Introduction

Numerous times have industrial accidents taken place with negative repercussions for both the environment and its inhabitants. Among the natural resources, water is the one most often directly affected. Being able to develop robust, real-time and cost-effective sensors for water monitoring is essential for ensuring a good quality of living. Various methods are developed to sense pollution with glass integrated photonics being among the most attractive solutions. On the one hand, it exhibits high sensitivity to absorption- or interferometry-based measurements and on the other it shows chemical compatibility with aqueous environments. An innovative idea for pollution detection is to assess the bacterial cellular viability as a global indicator for pollutant toxicity. Many sensors developed to detect and count bacteria involve a functionalization layer that is able to trap the desired molecules. This process however is both complex and expensive and also tends to reduce the lifetime of the sensor due to the layer's fragile nature. AC electrokinetics is an alternative method that is able to capture the target molecules by applying an AC signal on a pair of electrodes. It is a simple and reliable method that works in synergy with glass and integrated optics, which is characterized by its robustness, bio-compatibility and high sensitivity.

IMEP-LaHC is a laboratory internationally known for its work on glass integrated photonics that has been cooperating since a few years ago with biochemists to develop a sensor devoted to pollution monitoring. This report presents the results obtained on a first attempt to design and fabricate a glass integrated sensor co-integrating optics, AC electrokinetics and microfluidics. For this first study in a laboratory devoted to photonics but not to biochemistry, polystyrene latex beads have been used to model the dielectric behavior of the bacteria. This way safety in the conducted experiments is ensured. In order to reach the end goal, much exploration is necessary for both the underlying physics and the experimental processes. We need to bring on the same platform all the tools and knowledge for both manipulating the AC electrokinetics phenomena and characterizing the developed sensor. For this to be accomplished many separate steps are discussed, ranging from bibliography study, to electrodes/photonics design, to device fabrication, characterization and measurements. Having the aforementioned in mind, the current thesis is structured as follows.

In the first chapter, a way to detect industrial pollution is described as well as the qualities that the sensor must contain to fill the technological gap. Then, we proceed by presenting the laboratory and explain the reasons for which it is relevant for pushing the technology into the domain of optical bio-sensing further. Later, a brief review of the state-of-the-art is given and the objectives of the current master thesis are presented. Along with the objectives, a complete deconstruction and a Gantt diagram are detailed. Finally, in the last section we present the thesis outline.

In the second chapter, the most essential AC electrokinetics phenomena are introduced. Later, the electrodes design is studied in COMSOL in order to predict and explain the experimental findings. Finally, an integrated Mach-Zehnder interferometer is designed in order to maximize the sensitivity towards the target particles we want to detect.

In the third chapter, all the experimental processes along with their results are detailed. Information on the testbench, the process flow of the sensors, the preparation of particles is given. The AC electrokinetics experiments are conducted in order to trap and direct the target particles to the desired locations in a controllable and reproducible manner. At this section, we aim to complete a prototype that will be able to detect the captured particles.

In the forth and final chapter, the most important conclusions are given along with the perspectives, where we discuss about few potential paths to efficiently continue this project.

Contents

List of Abbreviations

AC = alternating current

ACEO = alternating current electro-osmosis

CM = Clausius Mossotti

DEP = dielectrophoresis

DI = deionized

EDL = electrical double layer

ETE = electrothermal effect

MZI = Mach-Zehnder interferometer

nDEP = negative dielectrophoresis

pDEP = positive dielectrophoresis

PDMS = polydimethylsiloxane

RGB = red-green-blue

SPR = surface plasmon resonance

Chapter 1

General Context and Objectives

1.1 Introduction

In this chapter, we begin by identifying the current need in terms of robust, real-time bio-sensing for water monitoring. We then proceed by describing IMEP-LaHC and its role into filling this gap with its integrated photonics technology. Afterwards, the state-of-the-art is presented in order to give a broad view of what is being researched today concerning optical bio-sensors. Following in the next section, the objective of this project along with its complete deconstruction are detailed. Finally, the Gantt diagram as well as the thesis outline are presented.

1.2 Fast, real-time bio-sensing: a necessity for the general well-being

Every year, numerous accidents take place in both industrial and natural environments causing much damage in both economy and human life. For instance in September 2019, a fire broke out at a Lubrizol factory in Rouen [1]. Due to the chemicals produced by the factory, the potential water pollution was a very serious consideration for the residents nearby. Unfortunately, it took a long time to evaluate the real amount of such pollution. In such cases, being able to react immediately and take countermeasures is crucial. A powerful testing method is to assess the bacterial viability, i.e. the survival of bacteria sensitive to a specific pollutant. The predominantly used "Pasteur method" for evaluating water pollution includes taking a sample and grow a culture in the laboratory. It is a complex process that requires several days [2] and it only provides an indirect measure. Despite the fact that several alternatives have been reported [3], there is still a significant margin of improvement in terms of speed, cost and real-time sensing.

Lab-on-Chip (LoC) systems are of particular interest for that matter as they are able to integrate many functionalities, bringing the conventional big laboratories on a single miniaturized device. This can result in portability, robustness, sensitivity, high diagnostic speed and automation at low cost. With their small size and low volume sample requirement, there is also a significant reduction in the usage of reagents and chemical waste, meeting the increasingly urgent environmental needs [4]. Moreover, with the proper utilization and control of the micro and nano-phenomena, engineers have a lot of tools to bring forward their vision. Several actuation mechanisms have been successfully reported, which are based on optics, magnetism, electrokinetics and piezoelectrics to name a few [5].

The development of optical biosensors is of considerable interest due to their high sensitivity, specificity and parallelization capacity. They support both label-based and label-free sensing with the latter being especially attractive. With labelling, extra enzymes and molecules (fluorescent or radioactive) are used to facilitate measurements, when the intrinsic properties of the target molecules are not sufficient for detection. This method is time-consuming and both labor- and cost- intensive and can alter the binding of the bio-receptors, introducing a systematic error to the bio-analysis [6].

Thus, a switch to label-free methods has been an ongoing process among the scientific community, with the optical biosensors being among its promising leaders.

The majority of label-free, optical biosensors involve the functionalization of the surface of the sensor on the grounds that it increases selectivity, sensitivity and performance. During this process, the surface of the sensor is chemically treated in order to change its properties and immobilize molecules, called antibodies, on top of it. The choice of these molecules is dependent on the target bacteria or virus we want to detect. For example, Giwan Seo et al. developed a functionalized field-effect-transistor-based biosensor to detect COVID-19 Causative Virus (SARS-CoV-2) [7]. As shown in figure 1.1, the surface of a graphene sheet is functionalized with antibodies that specifically bind SARS-COV-2 and activate the sensing mechanism of the device.

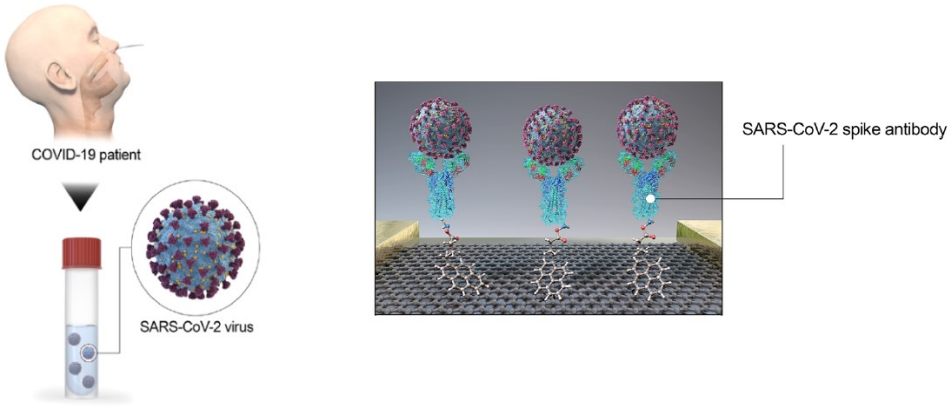

Figure 1.1: Immobilized antibodies on the sensor's surface bind SARS-CoV-2 [7]

The functionalization process however, proves an increasingly challenging problem with the scaling of the device and also induces an issue of properly cleaning after exposure. These result in increasing cost and complexity and in a potential reduction of the lifetime of the sensor, due to the fragile nature of the functionalization layer. Finally, it should be noted that in many cases during the functionalization process, many harsh chemicals are used with negative repercussions for the environment [8, 9].

Electrokinetics is an alternative way to trap the target molecules at the desired area without the need of functionalization. There are various phenomena that occur from the interaction of an electric field with the particles. For example, with electrophoresis the electric field acts through Coulomb force to charged particles. Dielectrophoresis (DEP) is on the other hand based on the interaction of the induced polarized dielectric particles with a non-uniform electric field. All these phenomena have come well to fruition, as in micro-scale forces can be significantly stronger. Moreover, electrokinetics only requires the design and fabrication of metallic electrodes and the choice of a proper voltage-frequency configuration, which makes up for a reliable and simple technology.

Indeed, alternating current (AC) electrokinetics, which includes dielectrophoresis and AC electroosmosis (ACEO), has been in the scope of research the last few decades [10]. They have shown significant promise in allowing functionalization-free, real-time sensing and along with the aforementioned strengths of photonics, will be one of the main cores of the present study.

1.3 IMEP-LaHC's incentive towards water monitoring

The Institute of Microelectronics, Electromagnetism and Photonics - Laboratory of hyperfrequency and characterization, IMEP-LaHC, is a mixed research unit (CNRS/Grenoble INP/UGA) that was founded in 2007 and is located in Grenoble-Minatec and Le Bourget du Lac. Its research activities are organized in three teams: Radiofrequencies and microwaves (RFM), Micro- and nanoelectronic devices (CMNE) and Photonics (PHOTO).

The laboratory hosts clean room facilities of class between 100 and 1000 and equipment for various other processes, such as ion-exchange on glass, silicon/glass processing (cutting, polishing, thinning, lapping) and more. In addition, it accommodates characterization benches dedicated to RF, integrated optics and micro-electrodes as well as software for simulation and design.

With its more than 40 years of experience in glass photonics, IMEP-LaHC is known internationally. Glass is a bio-compatible material with significant robustness and is able to withstand harsh and acid environments. Moreover, its transparency along with the parallelization capacity that glass photonics demonstrate, had led IMEP-LaHC into establishing and harnessing a complete set of tools for research and development.

Furthermore, over the last few years significant effort was put into establishing both the technology and knowledge needed in order to progress into the domain of optical biosensing. This includes partnerships with biologists, geologists and other experts as well as the necessary technology for the field. One example is the soft lithography and more notably, the polydimethylsiloxane (PDMS) fabrication, which is a core ingredient of many biosensors due to its properties and ease to both develop and prototype.

The present study, supervised by Elise Ghibaudo and Davide Bucci, researchers at the PHOTO group, aims to bring the already established expertise in optics and the biology together in order to develop a state-of-the-art integrated, AC electrokinetics-based, real-time, optical biosensor. It is a continuation of a work that started in spring 2020 by the then-master's student Léo Hetier [11]. In his work, Léo explored the phenomenon of dielectrophoresis, designed and simulated electrodes masks. Moreover, he studied the compatibility between the electrical and optical circuit in terms of optical losses.

Figure 1.2: Photo of Minatec campus where IMEP-LaHC is located

In the next section a brief literature review is given concerning label-free, optical biosensors. Even though AC electrokinetics is a main core of this project, functionalization-based sensors are also mentioned, in order to give to the reader a broader view on the most recent developments.

1.4 Label-free optics-based biosensors

Integrated photonics structures allow the transmission of light with minimal energy losses by confining the signal in waveguides. Waveguides are structures made of either dielectric or semiconductors with micronic or submicronic dimensions, that consist of a higher refractive index core compared to the surrounding media. They can be designed in such a way so that certain field distributions of electromagnetic waves, called guided modes, can propagate and confine the optical power in the proximity of the high-index core. The modes supported by the structures can be found by solving the Maxwell equations and by taking the continuity conditions in the interfaces of the waveguide. This means that both the surrounding environment of the core and the characteristics of the core itself (shape, dimensions, material) will determine the modes [12].

Depending on the wavelength of the injected light and the properties of both the waveguide and its environment, various propagation modes can be simultaneously excited. A waveguide can be designed in such a way that only the fundamental mode is supported, which is the guided mode that corresponds to the largest effective index. If this is accomplished, the waveguide is considered "single-mode".

Many optical sensors are based on the interaction of guided modes with external perturbations. This leads to a change in the propagation of the guided light which can then be sensed by a photodetector. One example of such sensors are those of evanescent field type. They are based on the interaction of the perturbation with the field distribution of a guided mode outside of the waveguide's core. As the evanescent field penetrates into the adjacent media for few hundreds of nanometers, any local changes of the substrate or superstrate, for example due to the presence of bacteria, will affect the guided modes. This will be translated to a change in the output intensity or phase in the propagation of light [13]. Some widespread devices that make use of this phenomenon include interferometers and surface plasmon resonance sensors (SPR), with the latter being one of the most widely used and commercialized.

Interferometers such as the Mach-Zehnder (MZI) are capable of extremely high sensitivity to the phase shift. The Mach-Zehnder consists of an input and output waveguide, two Y-junctions (called splitter and combiner) and two straight waveguides between the Y-junctions which are called "arms" (figure 1.3). There is the sensing arm where the perturbation takes place and the reference arm which remains unaffected. The light inserts the Mach-Zehnder, splits into the two arms and then recombines in the second Y-junction. Depending on the phase difference between the propagation modes in the measuring and reference arms, we can have either constructive or destructive interference [14]. Thus, any event that induces a phase difference between the two arms, is shown by a change of the intensity of light measured by the photodetector at the output.

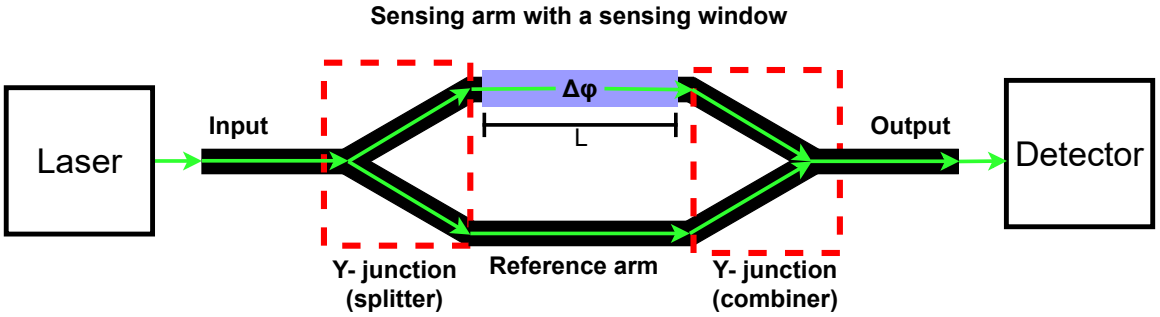

Figure 1.3: Schematic setup of a standard Mach-Zehnder interferometer.

An example of such event is the binding of bacteria on top of the sensing arm. Many bacteria and particles were successfully detected by this method. For example Mathesz et al. detected Escherichia coli. [15] whereas in other work, both Listeria monocytogenes [16] and streptavidin − biotin were able to be detected as well [17].

On the other hand, with surface plasmon resonance sensors, light is confined in surface plasmons which are surface electromagnetic waves that propagate at the interface of a metal and a dielectric. Surface plasmons show maximum amplitude at the interface and an evanescent field at the surrounding media. The excitation condition (resonance condition) of surface plasmons depends on local refractive index changes. This constitutes the sensing mechanism [18]. One example includes the functionalization of the sensor with bacteriophages for Escherichia coli and methicillin-resistant S. aureus detection, noting a limit of detection equal to 10^3 CFU/mL [19].

As far as AC electrokinetics is concerned, in 2019 Costella et al. developed a surface plasmon resonance sensor using AC electroosmosis and dielectrophoresis to trap human embryonic kidney cells or polystyrene latex beads [18]. In a more recent article, both functionalization and dielectrophoresis were suggested [20]. The combination of both phenomena may not get rid of the downsides of functionalization, but can increase the sensitivity even further, as in many cases the bottleneck of the sensor comes down to the diffusion-limited mass-transport of analytes to the surface and not to the limitations of the optical properties of the sensor. Thus, by applying AC electrokinetics, such as dielectrophoresis or AC electroosmosis, the analyte concentration near the surface increases and hence a better sensitivity is observed [18].

The table below contains all the aforementioned work, along with some other implementations regarding label-free, optical biosensors in order to give a more complete view on the matter.

Table 1.1: Various label-free optical sensors for biosensing. SPR: Surface Plasmon Resonance, MZI: Mach-Zehnder Interferometer, LoD: Limit of Detection, DEP: Dielectrophoresis, ACEO: Alternating current electroosmosis

Type of sensor	Substrate	Functionalization	AC electrokinetics	LoD	Target molecule	Year	Reference
SPR	Glass	Yes	No	10^3 CFU/mL	Eschericia Coli S. aureus	2012	[19]
SPR	Glass	No	DEP, ACEO	-	Latex beads Human embryonic kidney cells	2019	[18]
MZI	Glass	Yes	No	1.5×10^{-5} RIU	Streptavidin	2011	[17]
MZI	Glass	Yes	No	10^6 CFU/mL	Eschericia Coli	2015	[15]
MZI	Si	Yes	No	10^5 CFU/mL	Listeria monocytogenes	2014	[16]
Scattering	Glass	No	DEP	10^2 CFU/mL	Eschericia Coli	2021	[20]

1.5 Objectives of the internship

As it can be seen from table 1.1, optical sensors started integrating AC electrokinetics in their design. To the best of our effort, we have not found any research regarding integrated Mach-Zehnder on glass for biosensing applications, employing both AC electrokinetics and an integrated means of collecting the measurement signal.

This 25 weeks project is part of a bigger one (and will be followed by a PhD), where the end goal is to design a first prototype of a portable, microfluidic device for water monitoring, that will provide rapid, real-time results without a prohibitive cost and complexity (figure 1.4). The innovation lies on the utilization of AC electrokinetics for the trapping of the bacteria on top of the sensing arm of a Mach-Zehnder, with the application of an AC signal on the electrodes. The trapping will cause a change in the optical property of the Mach-Zehnder and a change in the intensity of light, which will be later captured and measured by the photodetector.

Towards this goal the following objectives are set:

1. Identify and understand the dynamics of AC electrokinetics.
2. Create a testbench that accommodates the tools for both the electrical biasing and fiber characterization.
3. Tune both bench and processes to clearly distinguish the particles under study.
4. Master the PDMS processes with respect to both creating it and bonding it on glass.
5. Study and implement electrodes on glass.
6. Trap in a reliable and reproducible manner the particles under study to the desired locations.
7. Create a functional optical bio-sensor with the implementation of a straight waveguide.
8. Create an interferometry-based optical bio-sensor with the implementation of a Mach-Zehnder.

In the next section, the more specific constituents of the general objective of this study are presented.

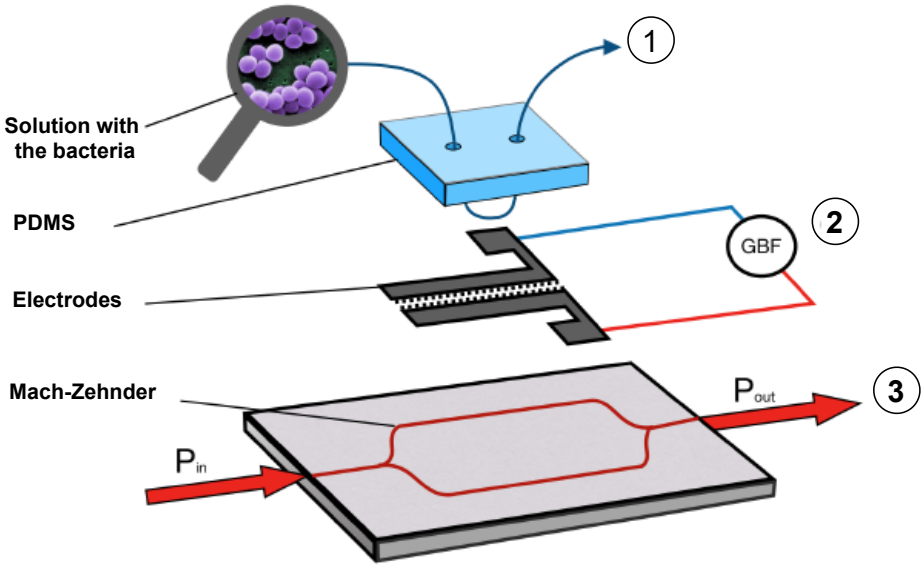

Figure 1.4: Schematic representation of the sensor [11]. (1) Microfluidic channel in which the solution with the bacteria will be injected (2) The electrical component where the AC signal will be applied to capture the bacteria (3) The optical circuit that will react by the presence of bacteria giving us the means to detect them.

1.6 Roadmap for the project

At figure 1.5, a breakdown of this study's objectives is shown. A glimpse of the priorities and the prerequisite steps of each process can be caught. All of the processes will be properly discussed later in the report.

As it can be seen from the schematic, at each stage many parallel processes are run. In the beginning, preparing the testbench for the experiments is of utmost importance. We need to bring together the electronics (for the application of AC electric fields), the optics (optical microscope for inspection as well as the tools for the alignment and fiber characterization) and the microfluidics. At the same time, the PDMS fabrication processes are explored and a first electrodes fabrication takes place by using a pre-existing mask drawn by Léo Hetier [11]. Finally, polystyrene latex beads are prepared and studied in the place of bacteria. This choice is made during the prototype phase because polystyrene latex beads can mimic the dielectric properties and the volume of bacteria on the one hand while allowing a safe manipulation on the other.

At the next stage, the AC electrokinetics must be studied, in order to find the best voltage-frequency values to maximize the trapping of the beads. This can be done in two ways, either by just depositing a droplet on top of the electrodes or by implementing a microfluidic channel to introduce the beads with a flow. At the same time, a study of the various electrodes designs will have already started, in case the results of the AC electrokinetics were found unpromising.

Once results on the trapping of latex beads by AC electrokinetics are available, by either the droplet-based experiments or with the implemented channel, the following are targeted:

1. Feedback to the electrodes design to correct or optimize the desired phenomena.
2. Development of a home-made script to analyze the latex-beads-related images taken with the optical microscope.
3. Once trapping is confirmed, a straight waveguide is implemented and a scattering/absorption-based optical sensor is developed.

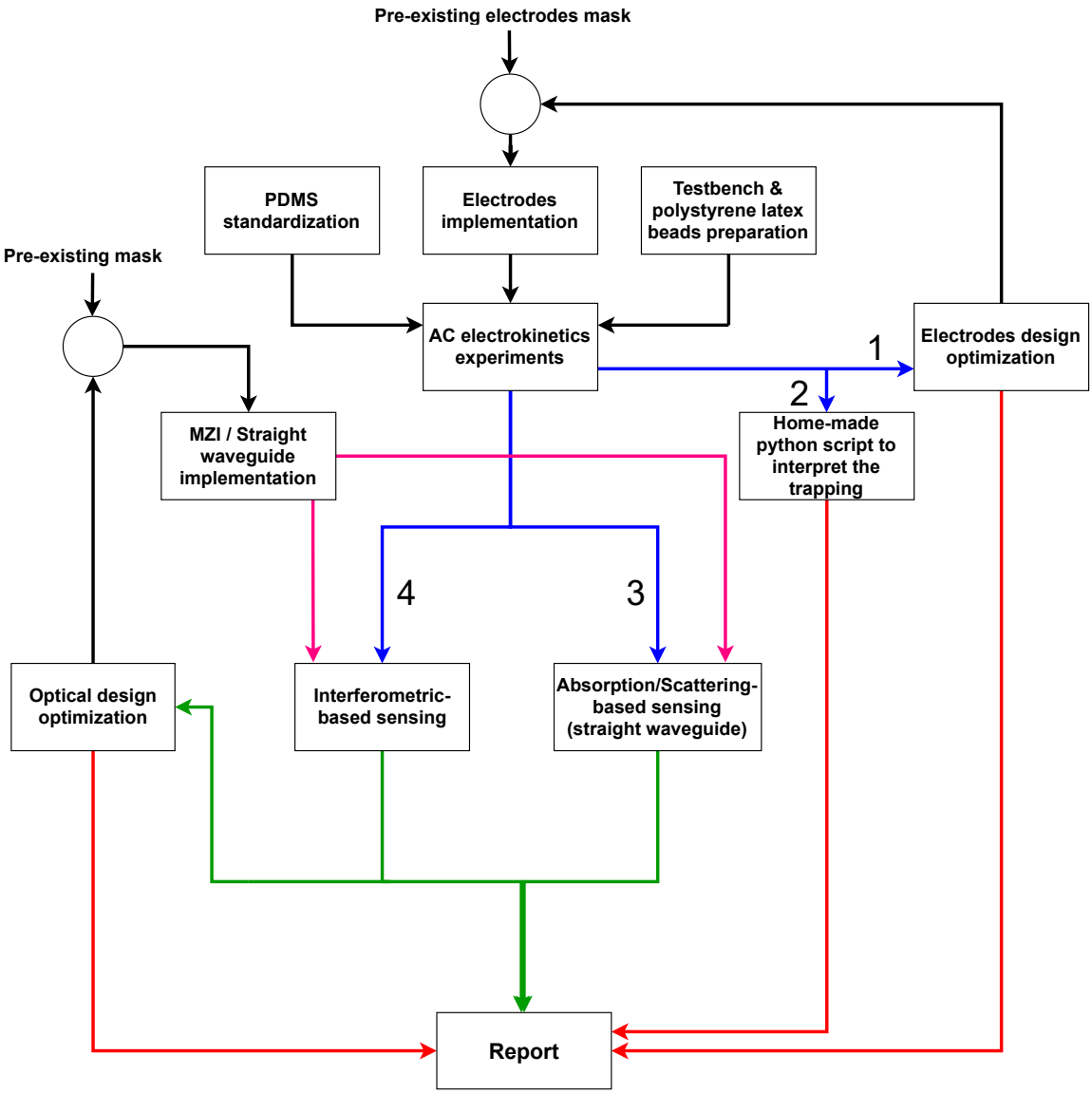

Figure 1.5: Schematic representation of the objective's breakdown

4. Once trapping is confirmed, a Mach-Zehnder is implemented and an interferometry-based optical sensor is developed.

Once the optical sensors are created, they are tested by biasing the electrodes and by using fibers to optically characterize them. At the same time, any newly gained information is used to optimize the design of the waveguides.

Even though the MZI is of higher importance concerning our end goals, slightly more attention is given on the straight waveguide as it is a simpler structure to study.

Finally, the most important findings from the experiments and the simulation are included in the report.

1.6.1 Gantt diagram

A Gantt diagram is presented below (figure 1.6) to supplement the aforementioned objectives' deconstruction.

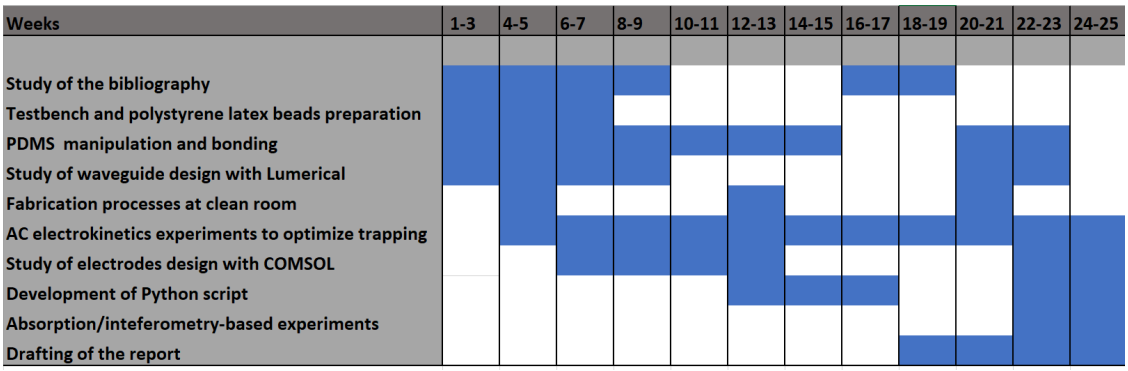

Figure 1.6: The Gantt diagram of the project.

At the next and final section of this chapter, the thesis outline is given.

1.7 Thesis Outline

In the second chapter, the theoretical background of the AC electrokinetics is formulated to describe all the relevant forces and their effect in terms of the applied frequency. In addition, the various geometrical parameters of the electrodes are simulated and studied in COMSOL, in order to find the appropriate design to maximize the dielectrophoretic forces and the trapping of the beads. Finally, the basic equations of a standard Mach-Zehnder are given and a simulation is detailed in order to optimize the sensing characteristics of the interferometer.

In the third chapter, the various experimental processes along with the results are presented. More specifically, we begin by describing the polystyrene latex beads and then we proceed in investigating the trapping of the latter on a device consisting of metallic electrodes on glass. Afterwards, an optical component (straight waveguide and Mach-Zehnder) is added, completing the prototype. Initially, slightly higher priority shall be given to the surface straight waveguide to both evaluate the quality of trapping and to ease ourselves to more complicated structures. Depending on the results and on the available time, interferometry-based sensing is explored by focusing on the Mach-Zehnder.

In the fourth and last chapter, a conclusion of this study is given, along with what should be the next steps in order to continue towards the end goal with the same momentum.

Chapter 2

AC Electrokinetics and Design

2.1 Introduction

In the previous chapter the importance of fabricating real-time biosensors for water monitoring was introduced. The promising role of AC electrokinetics as a tool to capture bacteria was mentioned and a bibliographic review was detailed. The objective is to use AC electrokinetics for the capture of polystyrene latex beads on top of either a straight waveguide or the sensing arm of an integrated Mach-Zehnder interferometer on glass. The captured beads' interaction with light will lead to a change in the intensity of the injected light which will be collected by the photodetector.

Therefore, the importance of understanding and properly manipulating the alternating current electrokinetics is significant for the detection of the beads. This is why at this chapter, we will begin by establishing the necessary theoretical background on the domain. More specifically, dielectrophoresis (DEP), alternating-current electroosmosis (ACEO) and the electrothermal effect (ETE) will be explained and a critical comparison will be made in terms of their dominance with regards to the applied frequency.

Afterwards, a COMSOL study will be presented regarding the electrodes used in this report's experiments. Various geometrical parameters will be investigated and the most relevant ones will be pinpointed in terms of their effect on dielectrophoresis and the trapping. Finally, the Mach-Zehnder interferometer will be discussed in more detail and the order of magnitude of the interaction length of the sensing arm will be calculated.

2.2 AC Electrokinetics

2.2.1 Dielectrophoresis

Dielectrophoresis is a phenomenon in which a force is exerted on a dielectric particle influenced by a non-uniform electric field. The electric field polarizes the particle and the resulting poles experience a force along the electric field lines, which can be either attractive or repulsive depending on the dipole's orientation. Therefore, by the non-uniformity of the electric field, a force of different magnitude will be felt by the particle's poles causing it to move.

The time-average dielectrophoretic force for a sphere is given by

$$F_{\mathrm{DEP}} = 2\pi\epsilon_{\mathrm{m}} r^3 \mathrm{Re}[f_{\mathrm{CM}}(\omega)]\nabla|E_{\mathrm{rms}}|^2 \tag{2.1}$$

where ϵ_{m} is the dielectric constant of the medium, r the radius of the particle, $\mathrm{Re}[f_{\mathrm{CM}}(\omega)]$ the real part of the Clausius-Mossotti (CM) factor and E_{rms} the root mean square value of the applied electric field [21].

The dipole's orientation and hence the direction of the DEP force is based on the relative polarization of the particle to the surrounding medium according to Maxwell–Wagner–Sillars polarization. It is described by the real part of the Clausius-Mossotti factor, $\mathrm{Re}[f_{\mathrm{CM}}]$.

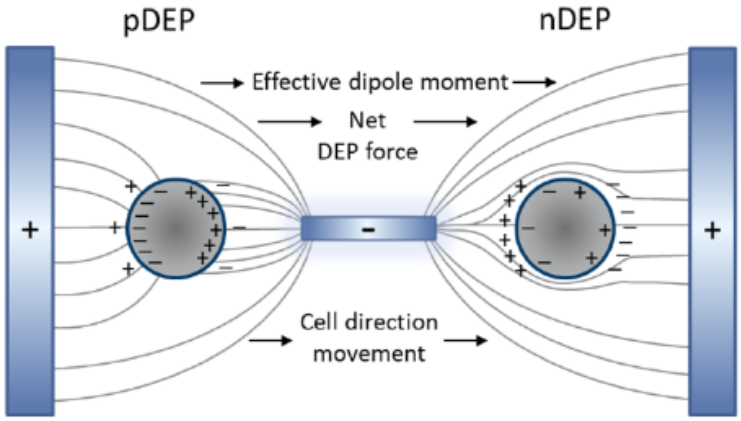

Figure 2.1: The effect of the relative polarization of the particle to the medium on the direction of the DEP force in a non-uniform electric field is shown[22]

The Clausius-Mossotti factor is defined as:

$$f_{\mathrm{CM}} = \frac{\epsilon_{\mathrm{p}}^* - \epsilon_{\mathrm{m}}^*}{\epsilon_{\mathrm{p}}^* + 2\epsilon_{\mathrm{m}}^*} \tag{2.2}$$

where ϵ_{p}^*, ϵ_{m}^* are the complex permittivities of the particle and medium respectively with $\epsilon_{\mathrm{p}}^* = \epsilon_{\mathrm{p}} - j\frac{\sigma_{\mathrm{p}}}{\omega}$ and $\epsilon_{\mathrm{m}}^* = \epsilon_{\mathrm{m}} - j\frac{\sigma_{\mathrm{m}}}{\omega}$. Here, ω denotes the angular frequency and ϵ_{m}, σ_{m} and ϵ_{p}, σ_{p} the permittivity-conductivity pair of the medium and particle respectively.

When the real part of the Clausius-Mossotti factor is positive, we have positive dielectrophoresis (pDEP) and hence the force is attractive, whereas for negative values we have negative dielectrophoresis (nDEP) and a repulsive force. This mechanism can be schematically shown in figure 2.1. On the left part, the particle is more polarizable with respect the medium, so the net dielectrophoretic force direction is towards the high electric field gradient. On the right part, the medium is more polarizable than the particle and the particle will move towards the low electric field gradient.

Effect of frequency

By taking the real part of the Clausius-Mossotti factor, we have the following two limiting cases regarding the applied frequency:

$$\mathrm{Re}\left[f_{\mathrm{CM}}(\omega \to 0)\right] = \frac{\sigma_{\mathrm{p}} - \sigma_{\mathrm{m}}}{\sigma_{\mathrm{p}} + 2\sigma_{\mathrm{m}}} \tag{2.3}$$

&

$$\mathrm{Re}\left[f_{\mathrm{CM}}(\omega \to \infty)\right] = \frac{\epsilon_{\mathrm{p}} - \epsilon_{\mathrm{m}}}{\epsilon_{\mathrm{p}} + 2\epsilon_{\mathrm{m}}} \tag{2.4}$$

Equations $2.3 - 2.4$ show that the magnitude and direction of the dielectrophoretic force is dependant on the conductivity of the particle and medium at low frequencies and on the permittivity at high ones. Moreover, what is of particular interest is the frequency that allows us to switch from pDEP to nDEP. This is found by taking $Re[f_{\mathrm{CM}}(\omega) = 0]$ and is given by:

$$\omega = \omega_{\mathrm{c}} = \sqrt{\frac{(\sigma_{\mathrm{m}} - \sigma_{\mathrm{p}})(\sigma_{\mathrm{p}} + 2\sigma_{\mathrm{m}})}{(\epsilon_{\mathrm{p}} - \epsilon_{\mathrm{m}})(\epsilon_{\mathrm{p}} + 2\epsilon_{\mathrm{m}})}} \tag{2.5}$$

More information on the math and the physics behind them, can be found in multiple sources [23]. In the next section, we are going to discuss about how to manipulate the Clausius-Mossotti factor and thus control the magnitude and direction of the DEP force.

Manipulation of Clausius-Mossotti factor

At the previous section we saw that by controlling the applied frequency or the conductivity/permittivity of the particle/medium, we can control both the direction and the strength of the applied dielectrophoretic force. This can open up many interesting applications such as the separation of live and dead cells. When the cell is dead, the membrane degrades causing an increase in the plasma membrane conductance which in turn changes the Clausius-Mossotti response to frequency [24]. This is illustrated in figure 2.2 (obtained from article [24]). At 7 kHz the live cells undergo pDEP whereas the dead nDEP, which means that they will be directed to different locations, as defined by the electrodes design. Thus, it becomes clear the importance of being able to calculate and tune the real part of the Clausius-Mossotti factor for the cells or bacteria that are under study.

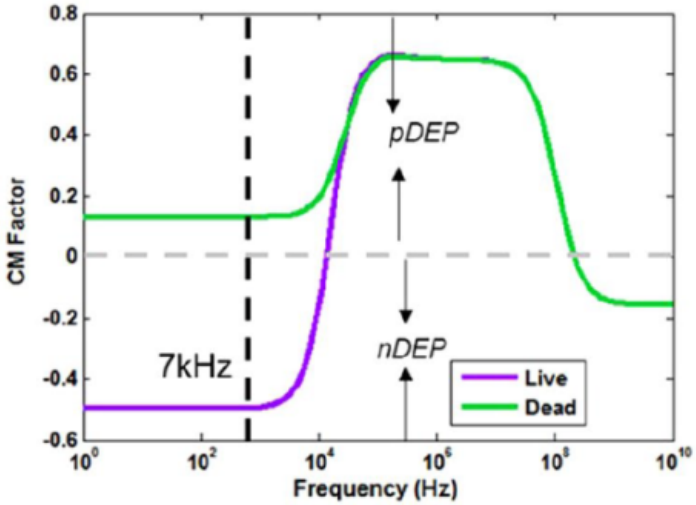

Figure 2.2: Clausius-Mossotti factor for live and dead HEK-293 cells in terms of frequency [24].

Apart from the frequency, the next easier way to control the Clausius-Mossotti factor is through the conductivity of the medium. For instance, salt can be added in water in order to increase its conductivity or a different medium can be chosen as well. However, in both cases attention must be paid on whether the studied bacteria can survive in the new conditions. For example, by adding salt, even though we may acquire the desired Clausius-Mossotti profile, the water activity may be reduced [25] to a degree that will prohibit the existence of the bacteria that we want to detect [26]. Therefore, the microbiological aspect has to be a part of the sensor's design.

An easy way to calculate the real part of the Clausius-Mossotti factor with respect to all the aforementioned parameters is by using "MyDEP" which is a free software made for DEP [27]. In figure 2.3, the real part of the Clausius-Mossotti factor is plotted with respect to frequency for different values of medium conductivity. In this example, the medium is deionized water ($\epsilon_{\mathrm{m}} = 78$) and the particles are polystyrene latex beads ($\sigma_{\mathrm{p}} = 2.1 \times 10^{-3}$ S/m, $\epsilon_{\mathrm{p}} = 2.56$). It can be seen that for these specific conditions, by increasing the conductivity, the plot is shifted downwards and at values of $\sigma_{\mathrm{m}} = 0.01$ S/m and above we have neither pDEP nor a crossover frequency. Therefore, no matter the applied frequency we can only have one state.

Before continuing to the next section, we need to point out that the presented theory and equations are based on the simple model of spherical particles as is the case with polystyrene latex beads. When dealing with real bacteria of various shapes however a more complex dielectrophoretic model should be established [28].

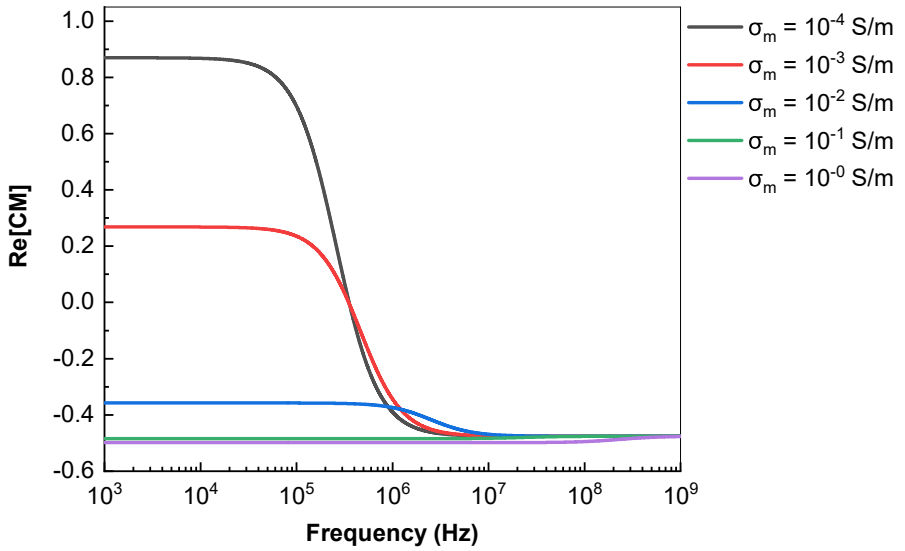

Figure 2.3: The effect of medium's conductivity on the real part of Clausius-Mossotti factor. Here $\sigma_{\mathrm{p}} = 2.1 \times 10^{-3}$ S/m, $\epsilon_{\mathrm{p}} = 2.56$ and $\epsilon_{\mathrm{m}} = 78$

2.2.2 Alternating Current Electro-osmosis

With the application of a potential on the electrodes, electrical charges accumulate on the electrodes' surface. These charges attract counter-ions from the medium (electrolytes) and thus two layers are formed. The first layer is called "Stern layer", and consists of counter-ions that are strongly absorbed on the surface charges. On the other hand, the outer layer, called "Diffusion layer", which spans a distance on the order of the Debye length, consists of weakly bounded ions that can move. These two layers comprise the electrical double layer (EDL) which is the mechanism on which alternating current electroosmosis is based [29].

In AC electroosmosis, the electrical double layer interacts with the tangential component of the applied electric field and an electrostatic force is produced that acts on the double layer and causes a fluid movement (figure 2.4). The rest of the fluid is dragged into motion due to the viscous forces. Regardless of the sign of the electrodes potential, the fluid direction remains the same, on the grounds that both the surface charge and the electrical double layer will follow the change of the electrodes' polarity. Thus the resulting force will retain the same direction [30].

The main difference between AC electroosmosis and classical electroosmosis lies on the existence of the surface charge. In classical electroosmosis, the surface charge is fixed and there is a linear relation between the applied voltage and the velocity. This is not the case for AC electroosmosis, where the electric field both induces and acts on the surface charges [31], resulting in a more complicated analysis.

Another key point to mention is that AC electroosmosis requires the existence of a non-uniform electric field and a pair of polarizable electrodes. The former is required in order to ensure the existence of a tangential component of the electric field [32]. The latter are needed in order for the electrical double layer to be created. In many cases during the analysis, it is considered acceptable to assume the ideal scenario of perfectly polarizable electrodes [31]. In that case, the electrodes constitute a capacitor where there is a clear charge separation at the electrode-electrolyte interface and hence there is no charge transfer between them.

As of now models are still being developed in order to study and predict the ACEO mechanism for various conditions. One of the most widely used assumes there is a linear relationship between the induced surface charge and the applied potential, while not taking into account the Stern layer at the same time [30].

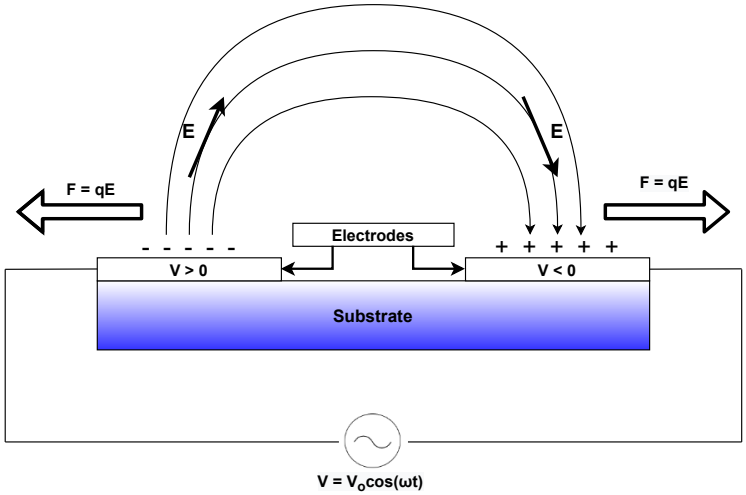

Figure 2.4: Working principle of alternating current electroosmosis (ACEO).

The velocity is given by

$$< V_{\text{ACEO}} >= \frac{\epsilon V_0^2 \Omega^2}{8\mu r(1+\Omega^2)^2} \tag{2.6}$$

where ϵ is the permittivity of the electrolyte (medium), V_o the applied potential at the electrodes, μ the viscosity of the electrolyte and r the distance from the center of the electrode gap. Ω is a non-dimensional frequency defined as:

$$\Omega = \frac{1}{2}\pi\kappa r \frac{\epsilon_{\text{m}}}{\sigma_{\text{m}}}\omega \tag{2.7}$$

where $\epsilon_{\text{m}}, \sigma_{\text{m}}$ are the permittivity and conductivity of the medium respectively, ω the angular frequency and κ the reciprocal Debye length [30].

From equations 2.6 and 2.7, we see that the velocity induced by AC electroosmosis:

- Is proportional to the applied voltage squared.
- Reaches a maximum value at the edge of the electrodes and a minimum at the center of the gap.
- Reaches a minimum value at low and high frequencies.
- Depends on the medium's properties (viscosity, permittivity, conductivity).

Effect of frequency

In order to explain the minimum value of the AC electroosmotic velocity at low and high frequencies, we need to go back to the physical explanation behind AC electroosmosis. This is the interaction of the tangential component of the applied electric field with the electrical double layer.

At low frequencies, there is enough time for space charges to screen the electric field, which results in most of the electric potential to drop on the double layers. That means that the tangential electric field outside the electrical double layer will be weak which will lead to very small velocities. On the other hand at high frequencies, the charges cannot keep up with the field, thus the charge of the electrical double layer is weak and the impedance across the electrolyte dominates [34].

This results in having a velocity profile in the form of a bell curve (figure 2.5) which falls almost to zero for low and high frequencies and reaches a maximum value at an intermediate one.

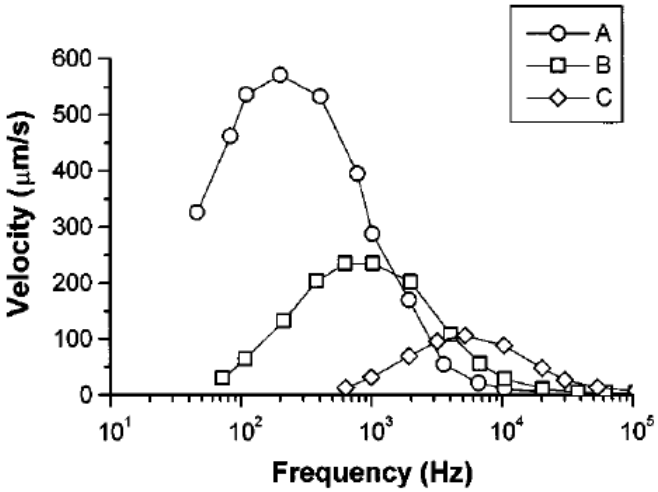

Figure 2.5: Line plot of the AC electroosmotic velocity with regards to frequency for three different medium conductivity values. A: 2.1 mS/m, B: 8.6 mS/m, C: 84 mS/m [33]

At the same figure, the effect of the medium's conductivity is shown as well. It can be seen that by increasing the medium's conductivity, the peak of the velocity appears at higher frequencies, but has a lower value. Thus, for insulating medium such as deionized water, the AC electroosmosis is expected to have a dominant effect at the lower frequency scale.

2.2.3 Electrothermal Effect

Electrothermal effect (ETE) is based on a temperature gradient in the bulk of the fluid in contrast to the electrode-electrolyte interface interactions in AC electroosmosis. The gradient can be a consequence of various phenomena such as Joule heating (internal) or even the induced heat from using the microscope (external). As a result of the temperature gradient, gradients in the electrical properties, such as conductivity or permittivity of the fluid, are also induced leading to the formation of free charges. These charges when acted by the applied non-uniform electric field will cause a flow which will drag the rest of the fluid by viscous forces [35]. When we are dealing with AC electric fields, this effect is called alternating current electrothermal effect (ACET)

Neglecting the fluid convection, the expression for the time-averaged electrothermal force per unit of volume can be derived [30]:

$$< \vec{F}_{\mathrm{ETE}} >= -0.5 \left[\left(\frac{\nabla\sigma}{\sigma} - \frac{\nabla\epsilon}{\epsilon} \right) \vec{E} \frac{\epsilon\vec{E}}{1+(\omega\tau)^2} + 0.5 \left|\vec{E}\right|^2 \nabla\epsilon \right] = 0.5\epsilon\nabla T\vec{E}^2\Pi(\omega) \tag{2.8}$$

where

$$\Pi(\omega) = \left(\frac{\alpha-\beta}{1+(\tau\omega)^2} - \frac{\alpha}{2} \right) \tag{2.9}$$

is a dimensionless function of frequency with:

- $\alpha = \frac{\nabla\epsilon}{\epsilon\nabla T}$, denotes the dependence of permittivity on the temperature gradient.
- $\beta = \frac{\nabla\sigma}{\sigma\nabla T}$, denotes the dependence of conductivity on the temperature gradient.
- ω, the angular frequency.
- τ, the charge relaxation time.

Information on the mathematical formulation can be found elsewhere [23]. The key points that are of interest is that the electrothermal force can reach a plateau for a wide range of frequencies [35] and that the direction of the force is determined by the Π parameter. For positive values, the flow is similar to the one in AC electroosmosis, whereas for negative value it takes the opposite direction [30].

2.2.4 Summary of AC electrokinetics

In the previous section a brief discussion was held regarding dielectrophoresis, AC electroosmosis and the electrothermal effect. These topics were discussed separately, but in reality most times at least two of them will coexist in the same system. Being able to estimate their dominance over each other at least with respect to a few parameters is of utmost importance. Table 2.1 summarizes our previous analysis to draw some conclusions.

Table 2.1: Summary of the main characteristic points of dielectrophoresis (DEP), AC electroosmosis (ACEO) and the electrothermal effect (ETE). In all cases, an application of a non-uniform AC electric field is assumed.

AC effect	Physical principle	Flow direction	Voltage dependency	Frequency dependency	Particle dependency	Medium dependency	Ref
DEP	Relative polarization of particle with respect to the medium	High gradient or Low gradient (electric field)	$\propto \nabla\left\|\vec{E}\right\|^2$	Varies	Size (r^3) conductivity permittivity	Conductivity Permittivity	[21]
ACEO	Formation of electric double layer	From edge towards center of electrodes	$\propto V^2$	Intermediate frequencies	No	Conductivity Permittivity Viscosity	[32, 30, 29]
ETE	Temperature gradient	Varies on properties	$\propto \vec{E^2}$	High frequencies	No	Conductivity Permittivity gradient permittivity gradient conductivity	[30, 35]

The most important distinction between these phenomena is that the size of the particles matters only for dielectrophoresis. It scales with r^3, which means that when dealing with bigger particles or bacteria, its effect is getting much stronger.

Another key difference is the behaviour of these forces with respect to the frequency. The electrothermal effect exhibits a steady effect for a wide range of frequencies, while AC electroosmosis is mostly strong at lower ones. Finally dielectrophoresis, depending on the Clausius-Mossotti factor, can reach a considerable amplitude both at low and high frequencies. So, it is safe to assume that at low frequencies in the order of $1 - 10^5 Hz$ the main competition will be between dielectrophoresis and AC electroosmosis, whereas at high frequencies it will be between dielectrophoresis and the electrothermal effect. Therefore, depending on the desired behavior of our system, an appropriate tuning could be made in favour of one of these forces.

The tuning can be also done in several other ways. For example, all of these forces depend on the medium's properties. Indicatively, an increase in medium's conductivity will result in a decrease of the AC electroosmotic velocity and an increase in the electrothermal effect. Being able to know which parameters matter and to what extend will help shift our focus and allocate time to the important from the very start.

Before proceeding to the next topic of discussion, we need to mention that there are various other forces present in the system. For example, there is the Brownian motion, buoyancy, gravity, drag forces and more. In most cases, with the range of voltages used, these forces can be ignored. However, they do have an effect and in some cases they must be considered into our calculations. For instance, in the work of Salari et al. it is mentioned that when there is an excessive temperature rise, meaning $\delta T > |\nabla T|$, the buoyant force dominates over the electrothermal effect [35]. Thus, ignoring it in favour of the latter could potentially produce inaccurate results.

In the following section, a thorough discussion on the electrodes design will take place by using a simulation software (COMSOL). The importance of this study can be seen from the fact that dielectrophoresis contrary to other forces, depends on the gradient of the electric field. Thus, if we want to reduce the other forces' effects, we can emphasize on the optimization of the electrodes, while keeping the applied voltage at a minimum. That way, both AC electroosmosis and the electrothermal effect especially will weaken considerably more.

2.3 Electrodes design

Our primary focus in this section will be on how to optimize the DEP effect. The main reason behind this choice is that DEP is more easily exploitable with regards to our end goal, which is to trap the bacteria/latex beads on the top of the sensing arm of the Mach-Zehnder or a straight waveguide.

More specifically, the goal of this analysis is to:

1. Pinpoint the trapping locations of polystyrene latex beads caused by dielectrophoresis.
2. Identify the most sensitive geometrical parameter affecting the DEP effect.
3. Understand what happens to particles that are located at a higher position compared to the electrodes.

2.3.1 Castellated Electrodes

Various electrodes geometries have been reported in the literature ranging from polynomial electrodes [36] to interdigitated [37] and three dimensional ones [38] to name a few. Each of these designs has its own merits and they can be used to favor either the nDEP or the pDEP, depending on the final objective. For example Petrovszki et al. developed electrode pair with tilted fingers to maximize the effect of pDEP [39].

Among the available design options, our primary focus will be to simulate castellated electrodes (figure 2.6) in order to both predict the expected DEP experiments and investigate how to enhance its effect. The motivation for this choice of geometry lies on the following:

- The existence of masks for castellated electrodes prepared by Léo Hetier [11].
- The extensive bibliography that implemented them.
- The simplicity to fabricate them with the laboratory's technology.

These masks were created but were not experimentally tested with DEP. Thus, simulating and finding the optimal choice of geometrical parameters would be a concurrent step along with the DEP experiments. This will help set a good basis to predict and explain the outcome of the experiments and find the general guidelines on how to enhance it.

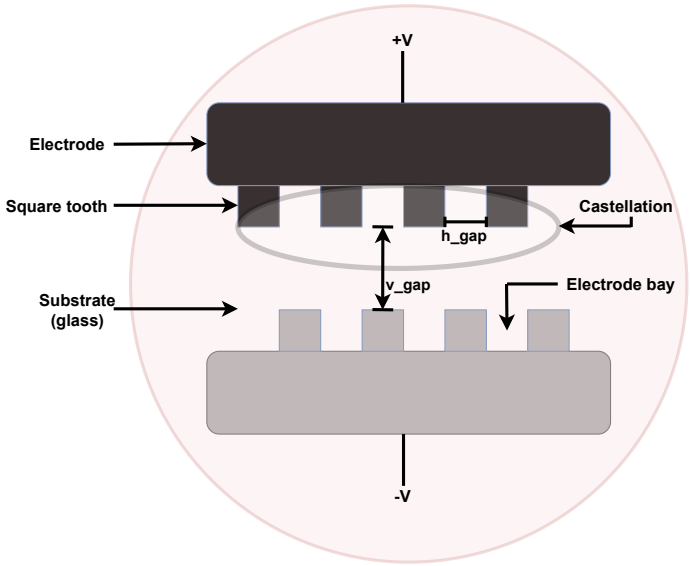

Figure 2.6: 2D sketch of the geometry of the castellated electrodes. The regions and parameters of interest are also defined.

2.3.2 Determination of the electric field distribution

As a first approach, the greatest portion of our analysis can be done in 2D. That way the computational needs will be reduced with respect to a full-3D approach. The first step will be to find the electric field distribution for the configuration shown in figure 2.6. For the simulation in COMSOL, from the AC/DC module the electrostatics interface was chosen with equations:

$$\vec{E} = \nabla V \tag{2.10}$$

$$\nabla \vec{D} = p_{\mathrm{v}} \tag{2.11}$$

$$\vec{D} = \epsilon_{\mathrm{o}} \epsilon_{\mathrm{r}} \vec{E} \tag{2.12}$$

where E the electric field, V the applied potential, D the electric displacement field, p_{v} the volume charge density, ϵ_{o} the permittivity of the vacuum and ϵ_{r} the relative permittivity of the medium. Even though DEP is predominantly an AC effect, electrostatics prove sufficient on the grounds that gives exactly the same electric field distribution, which is presented in figure 2.7. In this example, a potential difference of 20 V was applied and each square tooth was 50 x 50 μm. The gaps "v_gap" and "h_gap" were set at 50 μm as well.

The simulation results are in agreement with the experimental findings of many articles [40]. The non-uniformity of the electric field is shown along with the possible directions of the DEP force. In this configuration the particles under the effect of pDEP will gather at the edges of the electrodes' teeth and also in the middle taking a "zig-zag" shape. On the other hand, particles under the effect of nDEP will accumulate at the bays of the electrodes.

2.3.3 Study of the geometrical parameters

Gap between the electrodes

Previously as a starting value we used a gap ("v_gap" in figure 2.6) of 50 μm between the teeth of the electrodes pair. Now, we are going to investigate the effect it has on the electric field. The applied voltage and all the other geometrical parameters will remain fixed. The range of gaps that will be tested is 20 - 120 μm, with a step of 2 μm. For each gap, the electric field is sampled at a specific location shown with 'X' in figure 2.7. This will remain the same for the rest of the studies.

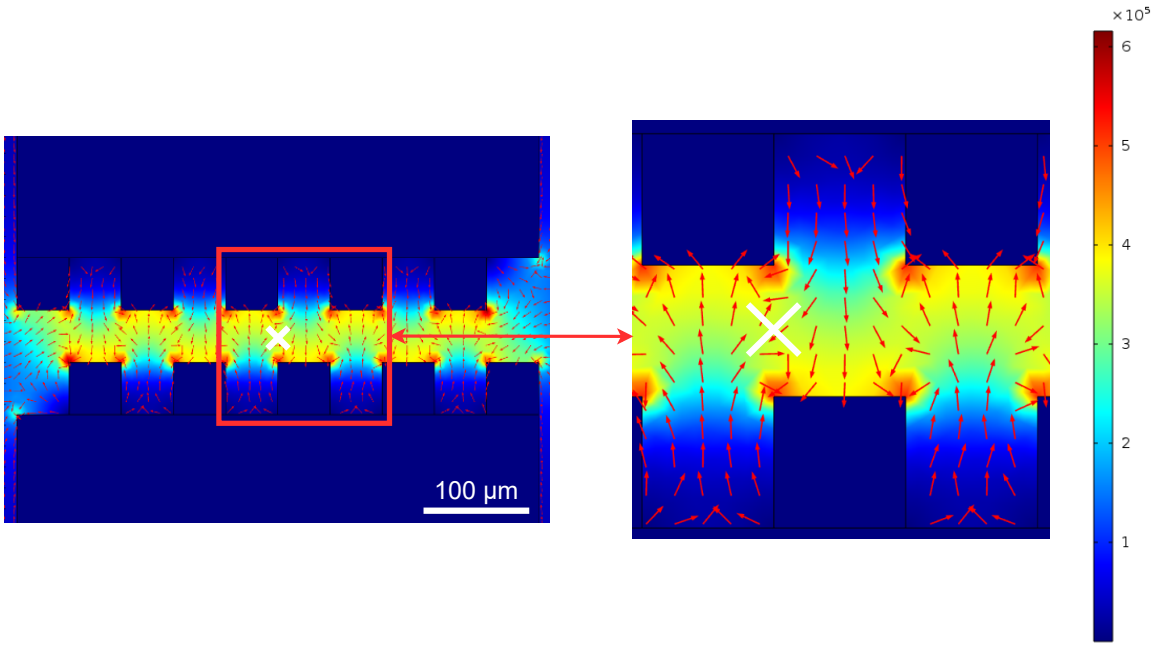

Figure 2.7: The electric field distribution for the castellated electrodes is shown. The arrows are normalized and they represent the direction of pDEP. Thus the tail of these arrows represent the direction of the nDEP. The 'X' represent the sampling point. For every parameter that we will study (gap, width etc.) only the electric field intensity on 'X' will be considered.

From the numerous such possible sampling points, this was the most interesting as it is placed in a representative region, where the waveguide is expected to be.

The results regarding the gap effect are shown in figure 2.8. A significant increase of electric field intensity for a reducing gap is observed. Indicatively, reducing the gap from 120 µm to 20 µm results in an increase in the order of 460%. Moreover, as DEP is dependant on the gradient of the electric field squared, the increase will be even more significant. However, the gap cannot be reduced as much as we want, as there must be sufficient space for the waveguide to lie in the middle, while keeping an adequate distance from the metallic electrodes at the same time [11].

Rest of geometrical parameters

Besides the gap between the electrodes, other geometrical parameters such as the horizontal gap ("h_gap") or the width of each tooth were individually inspected. The set of values used were in the range between 20-120 for the width of each tooth and 0-200 for the horizontal gap. In both cases, it was found that the intensity of the electric field is affected significantly less compared to the gap between the electrodes (less than 60% for the ranges used). Moreover, for horizontal gap close to zero the system would approximate two parallel rectangular electrodes of the same dimensions. Thus, the electric field between them would be uniform leading to a very weak gradient and hence dielectrophoretic force.

Therefore, among all geometrical parameters, the "v_gap" has a more significant effect with respect to the optimization of DEP and should be the first to optimize.

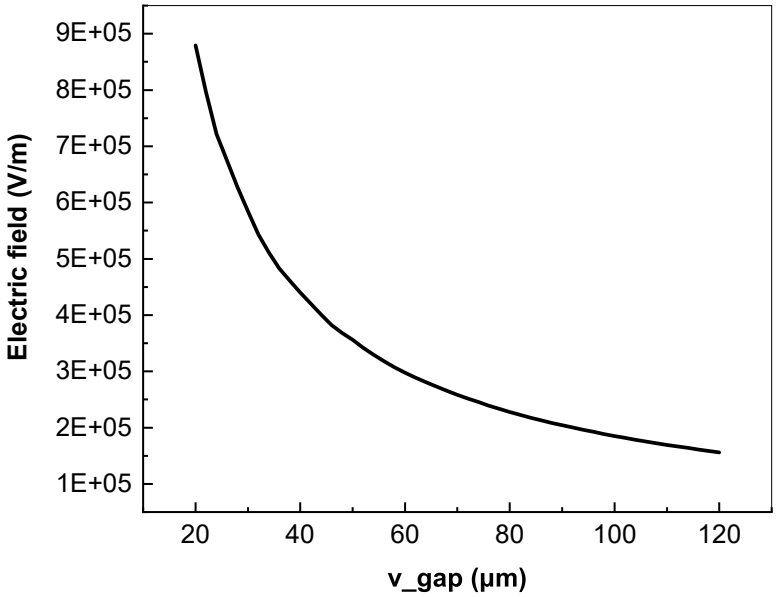

Figure 2.8: The effect of the gap between the electrodes on the intensity of the electric field at point 'X' is demonstrated. All other parameters remain fixed during the study.

2.3.4 Calculation of the electric field intensity in the vertical axis

In our previous analysis, a two-dimensional problem was considered. However, the real electrodes have a certain thickness and the electric field will extend to a certain height. This will be translated in the aggregation of particles in the vertical direction (z axis), one on top of the other. Even though, a big portion of our DEP experiments will involve an optical microscope which is able to capture only in 2D, there will be for sure an effect on the third axis as well.

In figure 2.9 (a, b) the electric field profile of a 2D plane on yz is presented. In this configuration the electrodes are made of aluminium with a thickness of 650 nm and are surrounded by air. In figure 2.9 (c), a plot of the electric field with respect to all the points in the z direction, denoted by the black line in (b), is presented.

We observe that the gradient of the electric field is stronger in a region ranging from the electrodes' height up to 15-20 μm above it, with an electric field intensity close to 1.63×10^5 V/m. This information indicates that in our final device beads that are located at a height of at least 15 μm above the electrodes, under the effect of dielectrophoresis will be directed downwards, directly on top of the surface waveguide.

This part concludes our study. First, we have managed to identify where the beads will aggregate under the influence of pDEP and nDEP. Second, we identified by simulations that the vertical gap between the electrodes is the most essential parameter to consider in our design. Finally, we saw that beads even 15-20 μm higher than the electrodes, will be directed by DEP towards the top of the waveguide.

It is important to note however that there are various others parameters that could be of interest. For example, Dalili et al. demonstrated that in the case of the existence of a microfluidic chamber, decreasing the height of the channel will result in a bigger effect of DEP [41]. Moreover, concerning their design, that of tilted planar electrodes, it was shown that there is a correlation between the height of the channel and the maximum value of the electrodes width for which we have an optimized DEP effect.

In addition, our presented model considered only the existence of DEP. Even though it is a common practice to consider and study these phenomena individually, in reality however we will

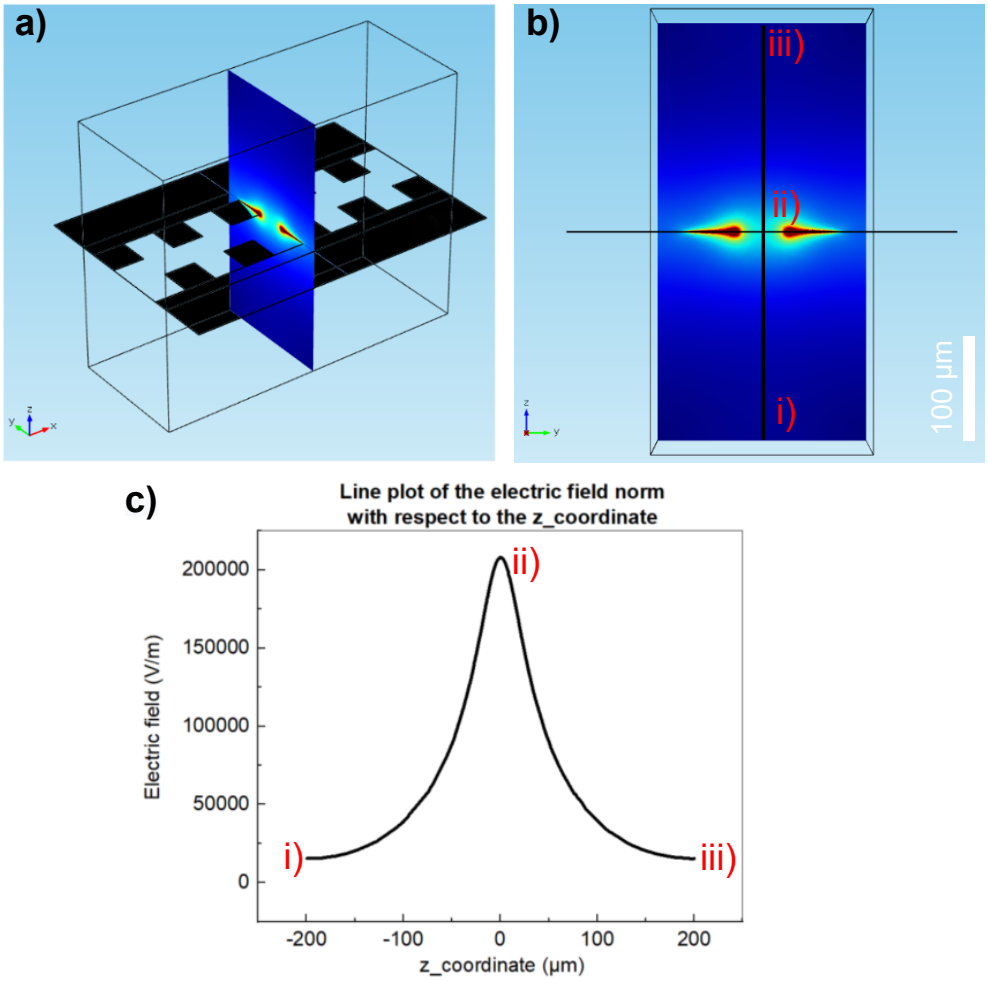

Figure 2.9: The electric field with respect to the z axis is presented. In the 3D model depicted in (a), a 2D plane is cut in the yz as shown. The plane is more clearly illustrated in (b). The black line was manually added and it represents all the points on which we will measure the electric field intensity. These measurements are included in a plot in (c).

have many simultaneous forces. Thus, in order to have a more precise picture of what is really happening, more forces should be taken into account. However, by tuning the frequency and the various other parameters to favor DEP, then our model will be a good approximation of the reality.

2.4 Mach-Zehnder Design

In the previous chapter we mentioned that a Mach-Zehnder consists of an input and an output waveguide, two Y-junctions (called splitter and combiner) and two straight waveguides between the two Y-junctions called sensing and reference arm respectively (figure 1.3). Monochromatic (single wavelength) and polarized light is coupled into the input waveguide and splits evenly in the two arms. The two guided modes propagate along the arms and finally recombine in the output junction. Based on external perturbations in the sensing window, a phase difference may be induced between them resulting in an intensity modulation caused by interference [42].

The intensity in the output is given by

$$I_{\text{out}} = \frac{I_{\text{in}}}{2}[1 + \cos(\Delta\phi(\delta\alpha))] \tag{2.13}$$

where I_{in} and I_{out} are the input and output power intensities and $\Delta\phi$ is the phase difference induced between the two propagating modes as a result of a change in a parameter of the sensing arm, $\delta\alpha$ [43].

The induced phase can be expressed as:

$$\Delta\phi = \frac{2\pi L}{\lambda}[N_{\text{s}}(\lambda, \alpha) - N_{\text{r}}(\lambda)] \tag{2.14}$$

where λ is the wavelength of the light, L the length of the sensing window and N_{s}, N_{r} the effective indexes of the propagating modes of the sensing and reference arm respectively [43].

2.4.1 Interaction length of the sensing arm

From equations 2.13 and 2.14 a problem of ambiguity (also known as "phase unwrapping") is observed [43]. Considering as an external perturbation the binding of latex beads on top of the waveguide for example, different concentrations may result in phase changes that differ an integer multiple of π. As a result, the same output intensity will be measured in the photodetector resulting in an ambiguity.

A way to solve this problem is to force a limit in the maximum value of the induced phase difference and design the system accordingly. By considering $\Delta\phi_{\text{max}} = \frac{\pi}{4}$ we can calculate from equation 2.14 the order of magnitude of the interaction length of the sensing arm: $L = \frac{\lambda\Delta\phi_{\text{max}}}{2\pi\Delta N}$. The choice of this value is made because on the one hand it faces the ambiguity problem and on the other because the cosine of an angle ranging from 0 to $\pi/4$ is not too far from its linear approximation.

The only unknown parameters in this case are the effective indexes of the propagating modes of the sensing and reference arm. We proceed to calculate these values by using the software Ansys Lumerical. We want not only to calculate these values, but also to design the system so that we are single-mode in all configurations shown in figure 2.10. A simplification that is made towards that is to assume that the trapped latex beads cover the whole surface of the sensing window.

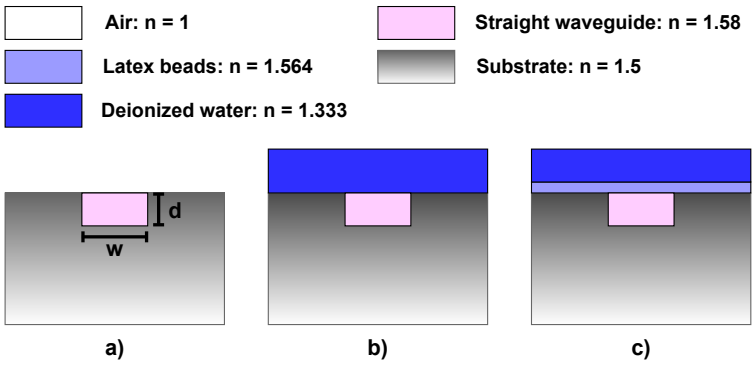

Figure 2.10: The straight waveguide will be designed (the width and depth will be defined) in order to be single-mode simultaneously in all of these structures. In (a) there is just air as a superstate. In (b) the superstrate is deionized water whereas in (c) it is composed of both latex beads that occupy the whole length and deionized water.

We start from a single waveguide and not immediately with the whole Mach-Zehnder to simplify our analysis. As long as the same geometrical parameters are used for all of the components of the Mach-Zehnder, the results can be applicable to the whole structure.

The substrate is considered infinite. In our system, both the sensing and the reference arm will be covered by deionized water, but only the sensing arm will be exposed to the particles under

study. The particles in this case, as mentioned in chapter 1, will be those of polystyrene latex beads. For the beads a layer of 0.9 μm was used, whereas for the deionized water a layer of 20 μm.

For a wavelength of 1.55 μm in order to be single-mode, the width and depth of the waveguide can be chosen to be 1.25 μm. We used the effective index method and an online solver [44] first to calculate a basis. Then, we tried a range of values around the basis with a more powerful software (Lumerical Mode Solution) until we got the desired result.

The effective indexes of the fundamental modes for the sensing and reference arm respectively are: $N_s = 1.526209$ and $N_r = 1.505690$. Substituting these values in equation 2.14 and assuming $\Delta\phi_{max} = \frac{\pi}{4}$ we find L = 9.44 μm.

This result however considers that the captured beads cover 100% of the area. This is very unlikely to happen, thus the maximum induced phase is expected to be less than $\frac{\pi}{4}$. This means that the resulting modulation of the intensity of the light may be less and thus make it harder to detect the trapped beads.

.

2.5 Conclusion

In the beginning of this chapter, the most basic AC electrokinetics phenomena were introduced. In addition, it was shown that frequency and the medium's properties among others, are of utmost importance to determine the range of their effect. More specifically, we saw that at low frequency there is a strong competition between dielectrophoresis and AC electroosmosis, whereas at high frequency between dielectrophoresis and the electrothermal effect. As each phenomenon affects the particles' movements in a different way, a proper tuning of all the parameters must be made in order to favor the one which will allow us to trap/direct the particles in the desired locations.

In the second part of the chapter, a modelling of the DEP took place in COMSOL. First, we identified the trapping locations of beads in the castellated electrodes and then we proceeded to investigate the various geometrical parameters. Among the parameters tested, we found that the most sensitive with regards to DEP effect is the vertical gap between the electrodes and thus this parameter should be the first to be optimized. Finally, the electric field distribution and its gradient were calculated in the z axis. We saw that beads located at a height 15-20 μm above the electrodes, under the influence of DEP will be directed downwards, on top of the waveguide.

Finally, in the third and final part, the basic equations of the standard Mach-Zehnder interferometer were given and the order of magnitude of the interaction length of the sensing arm for the case of the polystyrene latex beads was found to be 9.44 μm.

Chapter 3

Results and Discussion

3.1 Introduction

In the previous chapter, we started by building the basic background on AC electrokinetics. We then proceeded by investigating the castellated electrodes design and by pinpointing the expected trapping regions of latex beads. Finally, the working principle of a Mach-Zehnder interferometer was discussed and the order of magnitude of the interaction length was found for the case of polystyrene latex beads.

During this project, the experimental work was carried out in parallel along with the theoretical analysis. This possibility existed due to the existence of both electrodes and waveguides masks which allowed us to fabricate the devices from the very beginning [11]. This chapter presents the most essential experimental results, regarding the final objective to trap the polystyrene latex beads either on top of the sensing arm of the Mach-Zehnder or on a surface straight waveguide.

Initially, information on the preparation of the polystyrene latex beads is given. More specifically, the different kinds of beads used in the experiments and the different potential choices of medium for dilution will be detailed.

In the rest of the chapter, the results of the AC electrokinetics experiments are discussed. They are split into two sections depending on the kind of device used in the experiments. In the first one, the devices used consist of only metallic electrodes on glass and their main role is to study the AC electrokinetics and optimize dielectrophoresis and the trapping of the beads. During the analysis, a home-made Python script is also introduced to further explore the experimental findings.

After the trapping of the beads is verified, in the second section, devices with an added optical function are discussed. First a surface straight waveguide and then a Mach-Zehnder are implemented, constituting an absorption/scattering-based and interferometry-based optical bio-sensor respectively. In both cases, we will explore whether the trapped beads are able to change an optical property of the optical component to an extent that they can be detected. The straight waveguide is the first to be explored as it is a simpler structure to study.

In both kind of experiments, both the testbench and the process flow for the realization of the device are described.

3.2 Polystyrene latex beads preparation

Polystyrene latex beads are particles made from polymer that are in a stable dispersion in water [45, 46]. In our studies, two different kinds of beads are used:

- Latex beads, polystyrene - 3 μm (Sigma-Aldrich, LB30)
- Latex beads, carboxylate-modified polystyrene - 0.9 μm (Sigma-Aldrich, CLB9)

The main differences between these two categories is the size and the fact that the latter is charged due to the inclusion of carboxylate functional groups. The reason for dealing with both charged and uncharged beads is to mimic dead and viable bacteria respectively. In fact, when a cell dies, its membrane degrades and its conductivity increases considerably.

As these two kind of beads will be extensively mentioned in the report, a naming convention is proposed. From here on out, "uncharged" beads will refer to the first category (3 μm polystyrene latex beads) and "charged" to the second (0.9 μm carboxylate-modified polystyrene latex beads).

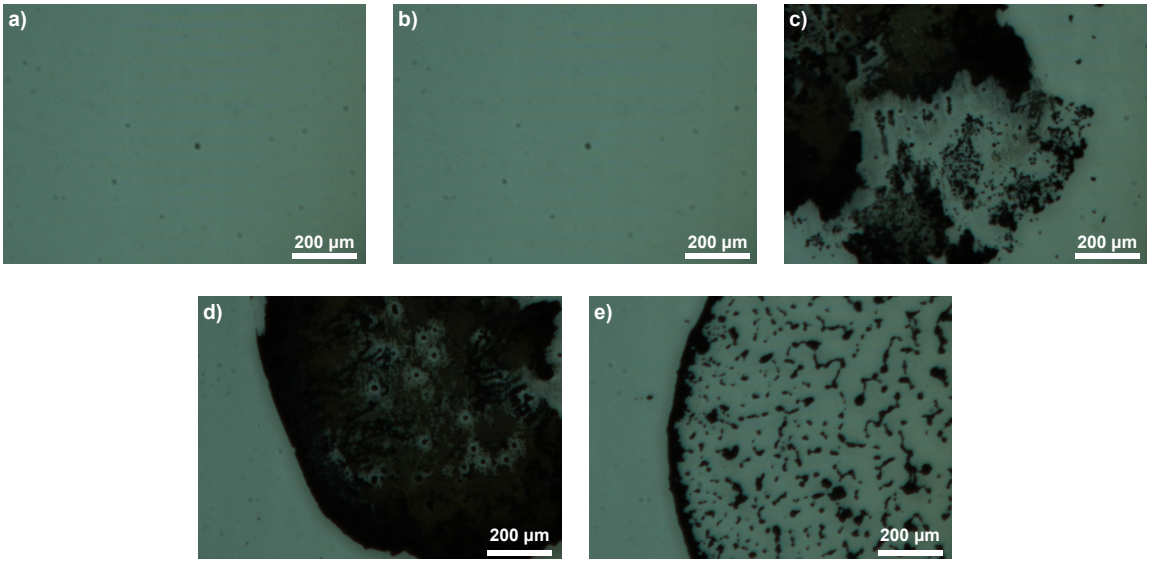

Figure 3.1: Images taken by an optical microscope on dried droplets of different qualities of water on top of a glass substrate: (a) clean substrate, (b) deionized water, (c) tap water, (d) tap water passing through a syringe filter, (e) Polystyrene beads diluted in deionized water. In all cases the same magnification was used (×170).

In the liquid suspensions sold by Aldrich, there is a very high concentration of beads and we need to dilute them. As both kinds of beads are dispersed in an aqueous suspension, the first choice was to dilute them further with water. Prior to the dilution, three different qualities of water were tested: tap water, filtered tap water (through a syringe filter) and deionized water. On a glass substrate one droplet of 2 μl for each of the three liquids was deposited. After the complete drying of the water, the areas were inspected with an optical microscope to judge the quality of the solution in terms of contaminants.

This inspection takes place due to the fact that latex beads are relatively small. In order to be clearly distinguishable, the medium's content should be devoid of particles of comparable, or bigger, size. In figure 3.1 the results are presented. The area where the droplet from the deionized water was dried remained unchanged (a, b). On the other hand, this was not the case for the other two (c, d). There were significant contaminants inside that filled the whole area. In the same figure, a droplet of polystyrene latex beads further diluted in deionized water was let to dry on the same glass substrate (e). Comparing the result to the one with just the deionized water (b) makes it clear that the beads are perfectly distinguishable. However, if we had chosen to use tap water or syringe-filtered water as the medium, this would not be the case. Therefore, for both charged and uncharged beads, deionized water has been our choice for the dilution.

3.3 Dielectrophoretic experiments on metallic electrodes on glass

The device used on the following experiments consists of castellated metallic electrodes on glass. The idea behind this is to create a simplified structure to study solely the AC electrokinetics and the dielectrophoresis especially. This device can be regarded as the prerequisite, exploratory step before proceeding to integrate anything else. More specifically the goals could be listed as such:

- Verify whether the trapping of the beads, in regions caused either by pDEP or nDEP, can be observed.
- Investigate the effects of voltage and frequency on the trapping, giving an emphasis on pDEP.
- Extract the crossover frequency.
- Compare the results with the theory/simulations.

3.3.1 Device fabrication

The process flow for the device used in this section is presented in figure 3.2.

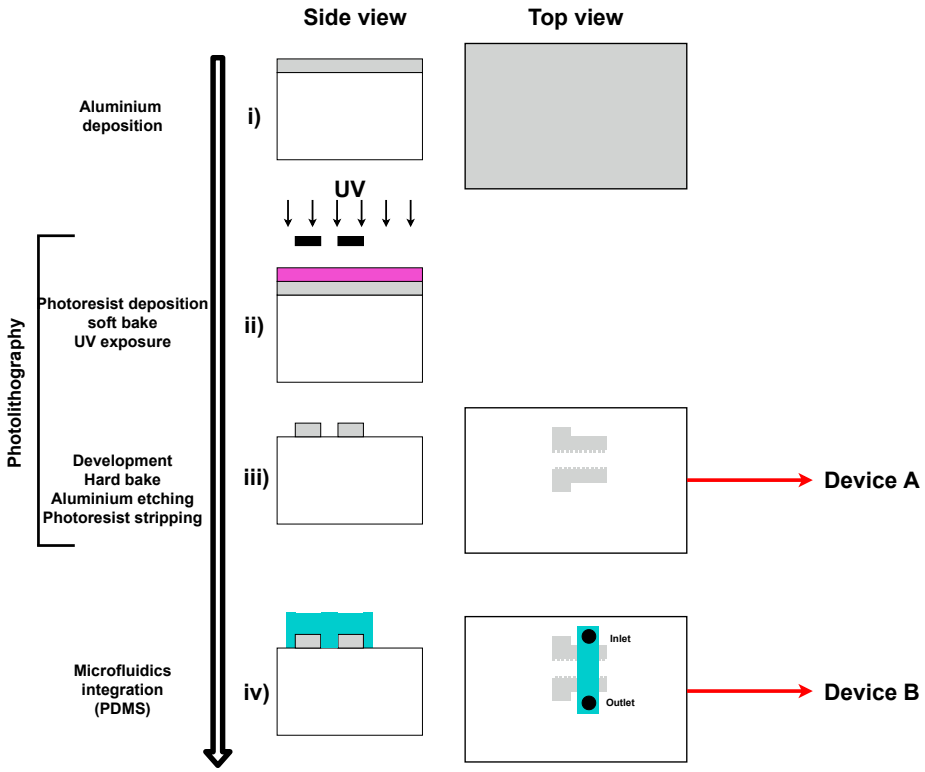

Figure 3.2: Process flow for the development of metallic castellated electrodes on glass.

For the fabrication of the metallic electrodes, standard photolithography processes are used [47, 48]. They involve depositing a photoresist on top of the aluminium and then exposing certain regions of it to UV light through a photolithography mask (ii). The exposed photoresist is developed revealing the aluminium underneath. Then, wet etching is performed which removes only the aluminium not protected by the photoresist. After the etching is complete, the residual unexposed photoresist is removed (iii). After the fabrication a microfluidic channel made of PDMS can be also added (iv) in order to accommodate the fluid with the sample (polystyrene latex beads).

In the fabricated device the dimensions of each tooth and the gaps "v_gap", "h_gap" are 50 μm (figure 2.6). Finally, when a PDMS microfluidic cover is added, the height of the channel is fixed by laboratory's technology at 39 μm. Regarding its other dimensions, their values may vary depending on the shape of the microfluidic encapsulation used.

3.3.2 Testbench

In figure 3.3 the testbench is presented. The sample is held by vacuum in a holder whose spatial position can be controlled with the micro-positioners. An optical microscope connected to a computer is on top and is able to capture and save both pictures and videos of the sample for various magnifications. An external illuminator light source is also used to illuminate the back of the sample in order for the optical microscope to capture more clearly the aggregated latex beads. A signal generator (max 20 MHz - 20 V_{pp}) is also present in order to bias the electrodes through very thin probes. Their movement can be also independently controlled.

A power amplifier allowing to obtain 30 V_{pp} for frequencies not higher than 100 kHz has been used in some cases as well.

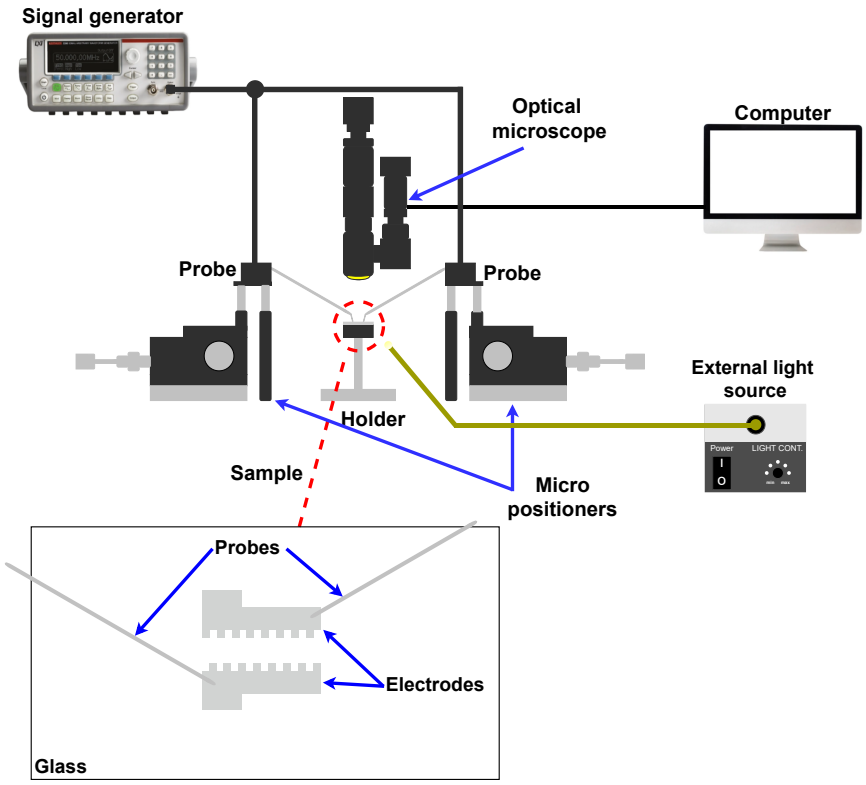

Figure 3.3: The testbench for the characterization of dielectrophoresis and a schematic of the sample, with the probes on the electrodes on top of the glass substrate.

3.3.3 Trapping of latex beads in the electrodes' bays

In order to capture the beads inside the bays of the electrodes, the nDEP must be the dominant force among the AC electrokinetics. According to theory, in the case of polystyrene latex beads, high frequencies are needed in order for the real part of the Clausius-Mossotti factor to be negative. The frequency range expected for nDEP for both charged and uncharged beads are higher than 1 MHz. This can be seen in the given example in figure 2.3. The available signal generator can only reach 20 MHz so higher frequencies could not be applied. To determine the

exact frequency values to obtain nDEP, information on both the medium (deionized water) and the particles' properties (permittivity, conductivity) are required. The information regarding the latex beads' properties has been estimated through articles. Due to the fact that each company fabricates the beads with its own processes, one cannot be certain of the relevance of these values. This does not apply to deionized water as much, as an extensive bibliography exists.

Uncharged beads

In the case of uncharged beads, trapping is observed at 10 kHz, which is much lower than the expected (few MHz). The trapping is very clear and lasts for the whole duration of the experiment prior to the complete drying of the droplet (figure 3.4 (a)). Even the theoretical triangular traps can be clearly distinguished which are in agreement with our simulations in chapter 2 (figure 2.7).

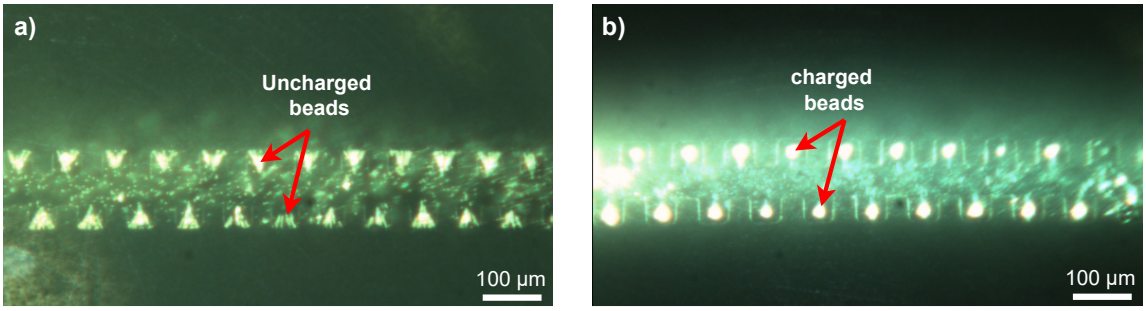

Figure 3.4: Images taken inside the droplet by the optical microscope. The dimensions of each tooth is 50 μm and the gaps "v_gap", "h_gap" (figure 2.6) are 50 μm as well. (a) The droplet contains uncharged beads (3 μm) which are trapped in the bays of the electrodes taking triangular shape. Voltage is 20 V_{pp} and frequency 10 kHz. (b) The droplet contains charged beads (0.9 μm) which are also trapped in the bays. Voltage is 20 V_{pp} and frequency 5 MHz. In both cases, the same electrodes and the same magnification are used.

What is of particular interest however, is that for higher frequencies ($\geq$ 30 kHz) the uncharged beads do not stay in the bays. If nDEP was the only existing mechanism, then the higher applied frequency would result in an either unchanged or stronger expression of the force. This was not the case in our experimental findings. Ascribing this to an increased dominance of the electrothermal effect, which is shown to be relevant in high frequencies, or perhaps to another existing phenomenon is not the only choice. As the beads' conductivity and permittivity values could not be experimentally measured in the laboratory but were taken from bibliographic research, it is also possible that they are not representing the reality. However, we believe that it is unlikely that the properties of the beads differ in such an extent between the companies that fabricated them. The real part of the Clausius-Mossotti factor is therefore not expected to be drastically different.

As a result, between the two hypothesis, the most plausible explanation in our view lies in the existence of another competing force, that starts getting stronger for frequencies higher than 10 kHz. This is also backed by the work of Oh et al. where they demonstrated that the $\Pi(\omega)$ factor associated to the electrothermal effect described in paragraph 2.2.3., has a linear relation with the electrothermal force (equation 2.8) and starts increasing after 10 kHz [30].

Charged beads

For the charged beads, it was observed that they could be trapped for frequencies above 2-3 MHz as expected (figure 3.4 (b)). However, after a few seconds, the beads would leave these traps and move presumably on top of the electrodes to other regions of low electric field gradient. One plausible reason behind this phenomenon is that other effects such as the electrothermal effect may start dominating at high values of frequency. In paragraph 2.2.3., it was mentioned that one plausible

direction for the latex beads under the electrothermal effect is from the edge of the electrodes to the center (exactly as in AC electroosmosis). This assumption is also backed by the fact that an external light source is used to see inside the droplet. The applied light is very bright and as a result temperature gradients are created that make the effect even more dominant. Moreover, relatively high voltages are used ($\sim 20V_{\text{pp}}$) which further enhance this phenomenon.

The reason of such a difference between charged and uncharged could also lie on the fact that uncharged beads have a diameter of 3 μm, to be compared with 0.9 μm of the charged ones. As mentioned in chapter 2, the DEP force scales with r^3, thus the bigger the particle, the stronger the force. In addition, nDEP in the case of uncharged beads may have reached its theoretical maximum value at the available frequencies contrary to the charged beads which may need higher values than what the generator can provide. In any case however for both kinds of beads the nDEP-based trapping in the electrodes' bays was observed and it is in agreement in terms of trapping localization with the COMSOL simulations in chapter 2 (figure 2.7).

3.3.4 Trapping of latex beads in the middle region

Previously, the effect of nDEP was demonstrated. Even though there is still room for improvement, especially in the case of charged beads, both kind of beads were successfully trapped in the desired locations, inside the bays of the electrodes. For the uncharged beads, the required frequency was 10-30 kHz, whereas for charged beads it was higher than 2 MHz. As promising as these results may seem, what is of utmost importance is the ability to trap the beads in the middle region between the electrodes, by appropriately tailoring pDEP. The reason for it is that underneath that area the sensing arm of the Mach-Zehnder, or simply a surface straight waveguide, will be located. It will be the main constituent of the working principle of the sensor. As a result, verifying and optimizing pDEP draws us closer to our objective.

Uncharged beads

During the experiments, the pDEP effect with uncharged beads was not successfully observed and the beads did not gather in the middle region. Frequencies in the range of $50 - 10^4$ Hz and voltages in the range of $1 - 30$ V_{pp} were tested, but to no avail. This does not necessarily mean that pDEP is not present but probably that AC electroosmosis is the dominant mechanism overshadowing DEP (paragraph 2.2.2). The motion of the beads, as recorded with the optical microscope, was in the form of vortexes in the electrodes edges and from the edges of the electrodes to the center, both of which are characteristic of the AC electroosmosis.

One way to work around this problem would be to find a way to shift the real part of the Clausius-Mossotti factor, and hence both pDEP and nDEP, to higher frequencies. That way AC electroosmosis could be less effective and pDEP could potentially manage to dominate and eventually lead to the trapping of the beads in the center. Increasing the conductivity of the beads has the potential to solve the problem, as was verified by using the "MyDEP" software (figure 3.5). In order to accomplish that however, one would need to dive deeply into surface chemistry in order to manage and find a stable way to increase the conductivity.

Charged beads

In the case of charged beads however, the scenery is different. The beads were successfully trapped in the middle region as shown in figure 3.6. The trapping is in agreement with the simulations conducted in COMSOL (figure 2.7). The applied signal was at 30 V_{pp} with a frequency of 50 kHz. A variety of voltage-frequency configurations could achieve this with the exception of very low frequencies in the order of few kHz, where once again AC electroosmosis dominates and no trapping is observed.

Even though a pair of values was found that could trap the beads, experimenting with different ranges is of significant interest as well. Experimenting with various excitation conditions could give an indication of the frequency after which AC electroosmosis stops dominating and of the frequency

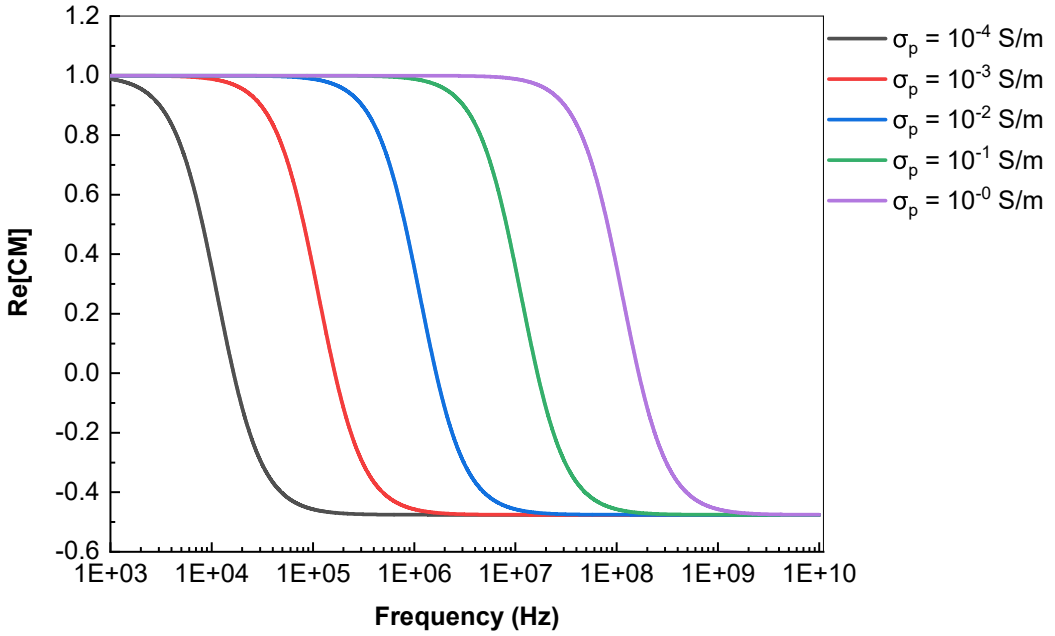

Figure 3.5: The effect of particles' conductivity on the real part of Clausius-Mossotti factor is shown. Here $\sigma_{\mathrm{m}} = 0$ S/m, $\epsilon_{\mathrm{p}} = 2.56$ and $\epsilon_{\mathrm{m}} = 78$

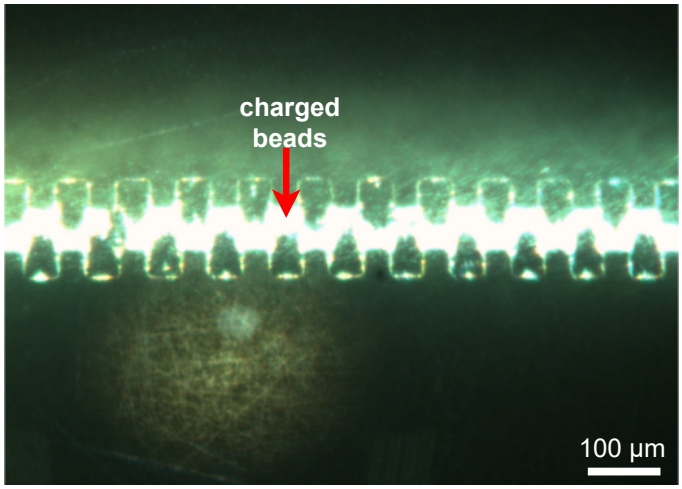

Figure 3.6: Image taken inside the droplet by the optical microscope. The dimensions of each tooth is 50 µm and the gaps "v_gap", "h_gap" (figure 2.6) are 50 µm as well. The droplet contains charged beads (0.9 µm) which are trapped in the middle of the electrodes taking the expected "zig-zag" shape. Voltage was set at 30 V_{pp} and frequency at 50 kHz.

after which pDEP starts deteriorating. In order to be able to extract this information, we will make use of a script written in Python that will be described in the next paragraph.

3.3.5 Analysis of the trapping

3.3.5.1 Script development for the quantification of the trapping

Information from the DEP experiments comes from images and videos captured by the optical microscope. This makes it difficult for the human eye to be able to recognize subtle differences between different amounts of trapping, speeds of trapping etc. This poses thus an obstacle in acquiring a thorough understanding of the effect of the applied signal in terms of either the voltage or the frequency.

A solution to this problem comes with the development of a script able to recognize even subtle differences in the beads' motion and on the trapping effects. The algorithm's logic can be seen in figure 3.7. The camera acquires a video of the trapping of beads by the DEP effect. From this video a still frame is periodically extracted (as defined by the user by using the VLC software) thus yielding hundreds of images that correspond to different moments of the experiment.

Before using the script, a preprocessing takes place: a region of interest is added by the user, the middle region (red box) in figure 3.7, corresponding to the expected region where beads will be collected by pDEP. It corresponds to the region where the waveguide will be placed, in the middle of the gap between electrodes. Once this region of interest is defined, the script automatically crops all the still frames and keeps only the area inside the red box.

As the beads have a slightly different color compared to their surroundings, a color discretization takes place. Once this is complete, all the beads in the images will have the same pixel value (Red-Green-Blue (RGB)). Then, the program calculates the area that the trapped beads occupy inside the red box by measuring how many pixels inside the red box have the same RGB values with the beads. The acquired number is then divided by the whole surface of the red box.

This calculated fraction, called "aggregation factor", is the tool to compare the various experiments. For example, in figure 3.7 we have images that correspond to different points in time during an AC electrokinetic experiment, where the applied voltage was $30\,V_{\mathrm{pp}}$ and the frequency 100 kHz. The algorithm takes as input hundreds of such images and gives in the output a graph plot. We can thus quantitatively treat the following points:

- How fast do the beads aggregate in the middle region?
- In which of the images, do we notice an efficient aggregation?

Two remarks shall be made regarding the developed algorithm:

1. In all images, in all experiments, for all the different voltage/frequency values, the red box must be ideally identical regarding both its location and its dimension. Otherwise, the fraction's efficiency as a tool of comparison will be diminished.
2. The optical microscope captures a 2D picture. As the script is based on such images, beads that are stacked on top of each other are not taken into account. Nonetheless, even with a 2D analysis, many useful remarks can still be made.

Duration of experiments

In most cases, an experiment is being analyzed by the developed script only for running time that satisfies $t \leq 1000$ seconds. The reason that a time restriction is added is inherent to the nature of the droplet-based experiments: The droplet will eventually dry and during the very last stages of drying, trapped beads are forced into the boundaries of the droplet (coffee stain effect). Moreover, another phenomenon induces a further restriction. During the drying process, the thickness of the droplet decreases and the focus of the optical microscope changes. This implies that the area enclosed in the red box is not constant throughout the experiment, introducing a systematic error in

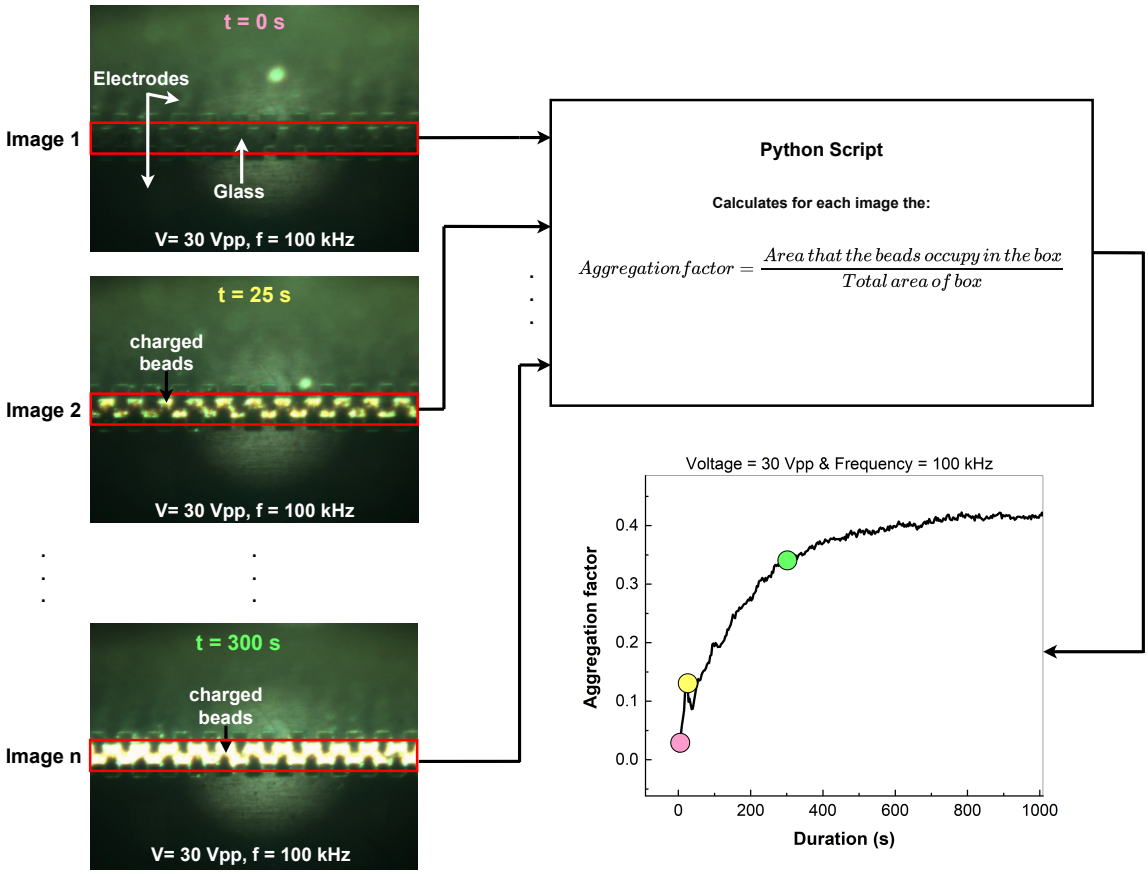

Figure 3.7: The developed script's logic is presented. Images are feeded into the algorithm along with the defined region of interest. The algorithm then proceeds to calculate the relative area the trapped beads occupy compared to the total area of interest.

our analysis. The error is assumed as systematic as at each experiment a droplet of constant volume is used (2 μl). Thus, the original thickness of the droplet and the time it needs to completely dry are fixed parameters. An acquisition time of 1000 seconds was chosen based on our observations on our experimental results.

Response time

Besides the "aggregation factor" (figure 3.7), another term that will be extensively used is defined:

- Response time: The time that is needed for the aggregation factor to reach the 90% of its maximum value, that was obtained for that specific voltage, frequency and running time of experiment.

This means that a saturation is not a necessary condition for the calculation of the response time, as we are not interested in the theoretical maximum of the aggregation factor, but on the maximum value that was observed during the experiment. Response time merely acts as a tool to compare the speed of the beads' accumulation in the regions of interest.

3.3.5.2 Evaluation of the crossover frequency of charged beads

Knowing the crossover frequency is vital to control the motion and therefore the trapping of the beads. Moreover, it allows us to have a first idea of the range of frequencies that could maximize

Cycle	$t_{start}(s)$	$t_{end}(s)$	Frequency	Is pDEP present?
1^{st}	0	25	25 kHz	Yes
-	25	50	5 MHz	No
2^{nd}	50	75	50 kHz	Yes
-	75	100	5 MHz	No
3^{rd}	100	125	100 kHz	Yes
-	125	150	5 MHz	No
4^{th}	150	175	200 kHz	Yes
-	175	200	5 MHz	No
5^{th}	200	225	400 kHz	Yes
-	225	250	5 MHz	No
6^{th}	250	275	800 kHz	Yes
-	275	300	5 MHz	No
7^{th}	300	325	1.6 MHz	No

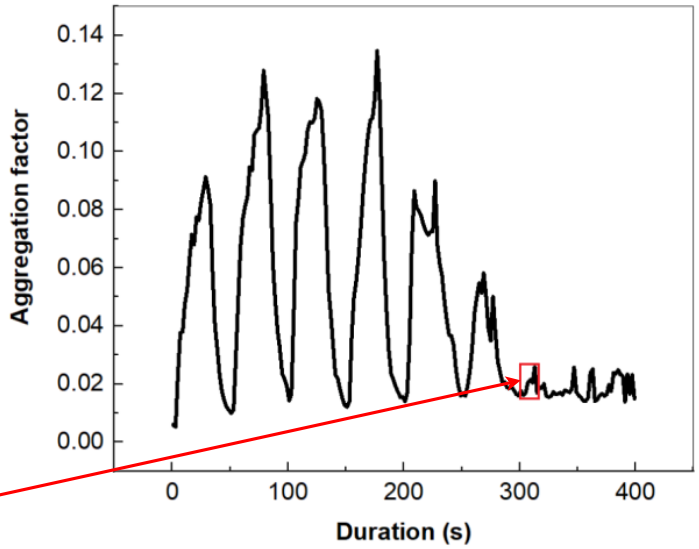

Figure 3.8: A set of applied frequencies (25 kHz - 1.6 MHz) alternated with a high frequency (5 MHz) are tested with regards to their effect on pDEP. If pDEP is present, beads start gathering in the central region and thus the aggregation factor increases. In case of nDEP (visible at 5 MHz), the beads leave the middle region and go towards the bays of the electrodes and thus the aggregation factor returns close to zero. In the left part of the figure, a table is presented to help illustrate the plot on the right better.

either pDEP or nDEP as it is known from theory (chapter 2), that frequencies close to the crossover frequency will have a weaker effect. Thus, by shifting to either lower or higher values that differ from the crossover frequency by an order of magnitude could be a promising first choice.

As seen in chapter 2 in equation 2.5, in order to calculate the crossover frequency that allows us to switch from pDEP to nDEP, both the medium's and the beads' properties are required. Since we do not have a reliable way to experimentally measure these values, an alternative direct method can be employed. This method is based on applying a set of frequencies in order to find the highest frequency for which pDEP is visible (f_{Phigh}) and the lowest frequency for which nDEP is visible (f_{nlow}). The crossover frequency will be between these two limits.

This experiment consists of many frequency cycles back to back. Each cycle involves the application of a frequency to cause a pDEP effect, followed by a high frequency (5 MHz) to cause nDEP. In all cycles, only the first applied frequency was changed. The second applied was always 5 MHz. The frequency set is scanned until a frequency is found where pDEP is no more observable.

This is better illustrated by the graph in figure 3.8. If pDEP is present and dominant, then the charged beads will start gathering in the middle region (as defined in the red box in figure 3.7). This means that the aggregation factor will start increasing. At nDEP, beads from the middle region will go to the bays of the electrodes as was shown in figure 3.4, thus resetting the value of the aggregation factor to theoretically zero.

From figure 3.8 it is observed that for a frequency equal to 1.6 MHz we have no pDEP and thus no accumulation of beads to the central region. This means that the highest frequency for which pDEP is visible is at the previous cycle and it is found equal to 0.8 MHz. Regarding the nDEP, the lowest frequency for which we have nDEP was already found experimentally close to 2 MHz. Thus we have: $f_{\text{Phigh}} < f_{\text{crossover}} < f_{\text{nlow}} \Rightarrow f_{\text{crossover}} \in (0.8, 2)$ MHz. In order to verify this result, a bibliographic research should be conducted.

In the work of Vahey et al. an estimation on the conductivity of the 0.9 μm charged beads can be obtained [49]. More specifically, it is stated that the electrical conductivity of polystyrene

beads can be calculated as:

$$\sigma_{\mathrm{p}} = \sigma_{\mathrm{bulk}} + \frac{2K_{\mathrm{s}}}{\alpha} \tag{3.1}$$

where σ_{bulk} the bulk conductivity, K_{s} the surface conductance and α the particle radius which in our case is equal to 0.45 μm. By ignoring the bulk conductivity and taking $K_{\mathrm{s}} = 2.27$ nS we get $\sigma_{\mathrm{p}} = 10.08$ S/m. Considering the conductivity and permittivity of deionized water equal to 2×10^{-4} S/m and 78 respectively [50] and the permittivity of latex beads equal to 2.56 [18], by using the "MyDEP" software we calculate $f_{\mathrm{crossover}} = 1.67 \in (0.8, 2)$ MHz. This value is in agreement with the range found through our experiments.

In addition to the crossover frequency, from the plot in figure 3.8 it is observed that the highest peaks are for frequencies in the range of 50 - 200 kHz. Outside this range, the peaks decrease and after 800 kHz they completely disappear. This means that the force of pDEP is weaker and less beads accumulate in the central region. As each cycle lasts only 50 seconds, however, it cannot be concluded from the graph, whether all these frequencies had the potential of maximizing the aggregation factor. In other words, it cannot be deduced from this graph whether these peaks indicate not only an effect on the speed of accumulation but also on the maximal occupancy by the beads. Nonetheless, it does indicate that the pDEP seems to dominate AC electroosmosis in the range of 25-800 kHz, which was one of our main objectives.

3.3.5.3 Effect of the applied frequency

In the previous section, an effect of the frequency on the speed of accumulation has been shown. However its effect on the maximum value of aggregation factor could not be deduced, due to the shortness of the experiment's cycles. In order to shed some light on this, three experiments were conducted for each of the best performing frequencies in figure 3.8: 50, 100 & 200 kHz. In all experiments, voltage was fixed at 20 V_{pp}. Each of these frequencies' effect was tested three times in order to evaluate both the repeatability and the reliability of our findings. The results are presented in figure 3.9. The first thing we noticed is that the application of 50 kHz leads to a much weaker aggregation factor compared to the other two frequencies which appears similar in their effect. This verifies our previous concern that the results in figure 3.8 were mainly demonstrating the effect of frequencies on the speed of aggregation and not on the maximum surface area that can be eventually occupied.

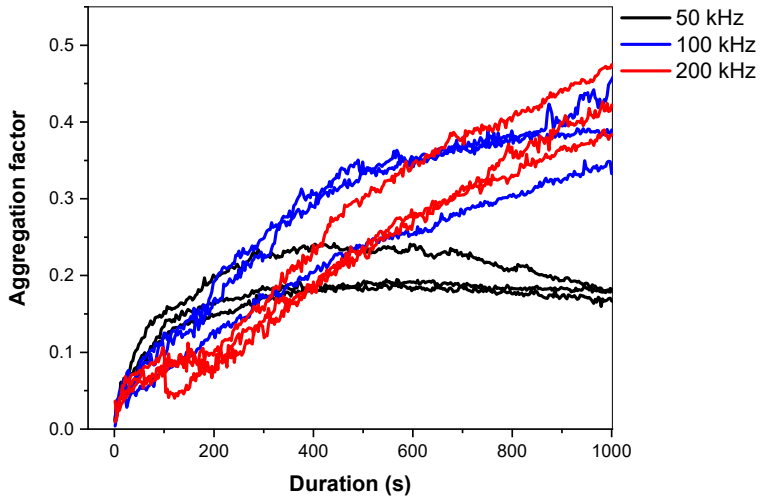

Figure 3.9: The line plot of the aggregation factor with respect to time for different frequencies. In all cases voltage is fixed at 20 V_{pp}. Each frequency value is tested three times.

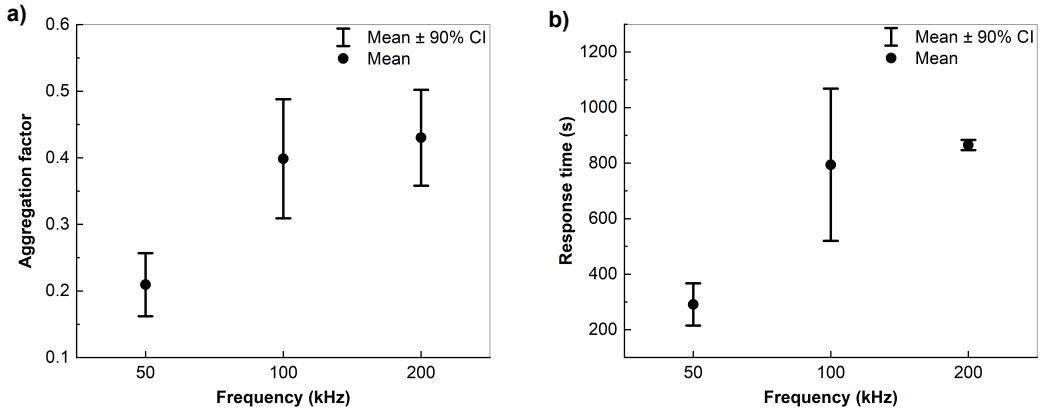

Figure 3.10: (a): Interval plot of the aggregation factor with respect to frequency. (b): Interval plot of the response time with respect to frequency. A voltage of 20 V_{pp} is applied in all cases and a confidence of 90% is used. For each interval, three experiments were made under the same conditions.

In figure 3.9 we can see that all measurements done at 50 kHz reach the saturation point earlier and then due to the drying forces and the shift of focus that was mentioned in 3.3.5.1, the value is decreasing. This is more apparent in the second repetition, where a considerably higher peak is observed compared to the other two. This behavior of the 50 kHz measurements differ from the other two frequencies, where the saturation of the aggregation factor is not yet reached and thus the maximum value for the 100 and 200 kHz is found close to t = 1000 s.

In figure 3.10 the interval plots with 90% confidence of the aggregation factor and the response time for different frequencies at 20 V_{pp} are presented. We observe that at 50 kHz the response time is considerably smaller as in the case of 100 and 200 kHz, saturation is not yet reached. And on the contrary, the aggregation factor for the two higher frequencies is a lot higher.

In our case, aggregation factor plays a more important role compared to the response time. The final device will depend on beads reaching the waveguide. Only when this is guaranteed, the response time can be taken into account. Otherwise, the optical sensor will not work as intended. Therefore, in the following experiments either 100 or 200 kHz will be used.

3.3.5.4 Effect of the applied voltage

In the previous sections the crossover frequency was estimated and the effect of frequencies, ranging from 25 kHz to 1.6 MHz, on the strength of pDEP was shown. It is known from chapter 2, that the higher the voltage the stronger the DEP effect, but we do not know yet exactly what effect it has on either the aggregation factor or the speed of accumulation.

In figure 3.11 the results of nine experiments are presented. For a frequency of 100 kHz, three different voltages were tested: 10, 20 and 30 V_{pp}. Each experiment was repeated three times in order to test the repeatability and reliability of the results. With respect to 10 V_{pp}, for both 20 and 30 V_{pp}, a much bigger area is occupied by the beads and considerably faster as well. A plateau is reached only in the case of 30 V_{pp} as the DEP effect is stronger and the process of aggregation faster. Regarding the variation, in the case of 20 V_{pp} a higher value is observed. These results can be illustrated by the interval plots in figure 3.12.

The increased variation for the 20 V_{pp} which is shown by the height of each interval is more visible in this figure. This could be ascribed to the lack of standardization of the experiments. A conclusive remark cannot be made, as the variation could either disappear or match the others, had we increased the number of tests done per voltage.

Based on these results, it seems that in case a very fast response is required, a high voltage can be used. For example at 30 V_{pp}, saturation is always reached with the response time being

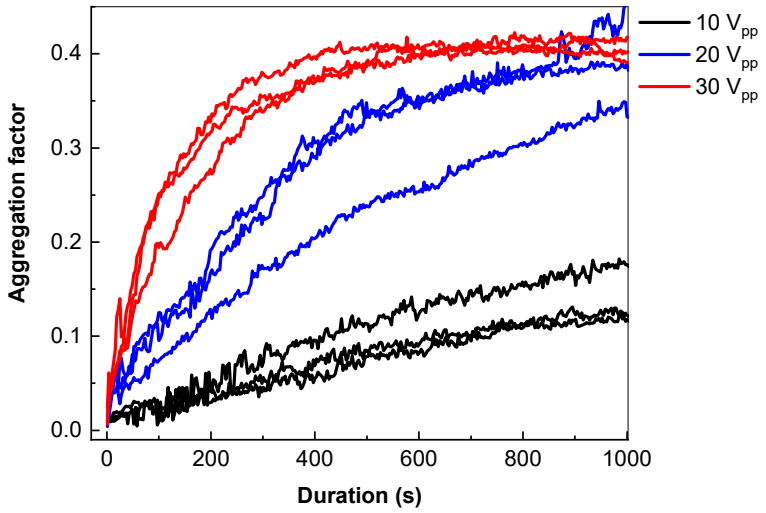

Figure 3.11: The line plot of the aggregation factor with respect to time for different voltages is presented. In all cases frequency is fixed at 100 kHz. Each voltage value is tested three times.

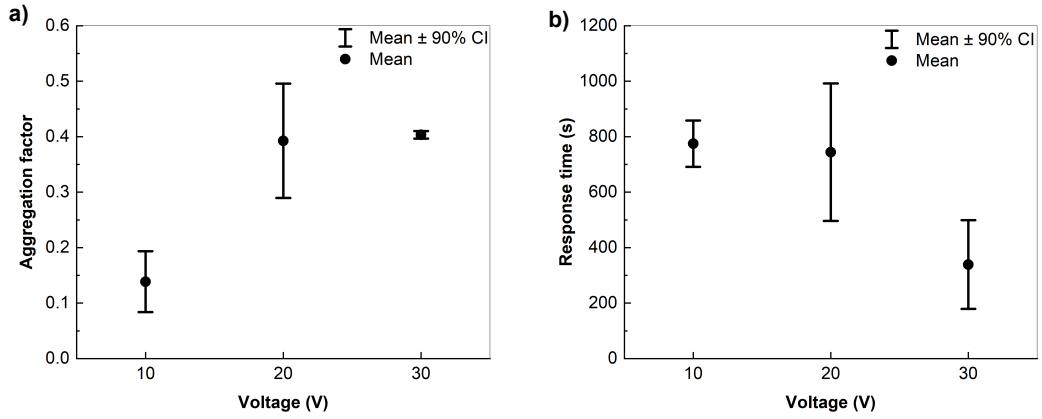

Figure 3.12: (a): Interval plot of the aggregation factor with respect to voltage. (b): Interval plot of the response time with respect to voltage. A frequency of 100 kHz and a confidence interval of 90% is applied in all cases. For each interval three measurements were done under the same conditions.

approximately 50% faster compared to 20 V_{pp} needing 339 seconds instead of 744. In addition, it is seen that for both 20 and 30 V_{pp} a similar maximum aggregation factor is noted which is considerably larger than in the case of 10 V_{pp}.

Knowing which configuration will be the optimal one will depend on the specifications of the design, on any power constraints and on the relation of the aggregation factor with the sensitivity of the Mach-Zehnder interferometer.

This concludes our droplet-based experiments. Both the nDEP and the pDEP effects were verified for the charged beads, which in turn verify our COMSOL simulations' results in chapter 2. The crossover frequency was experimentally estimated. In addition, the effect of voltage and frequency was found with regard to the pDEP. For a frequency equal to either 100 or 200 kHz, the effect of pDEP is maximized and dominates AC electroosmosis. Concerning the voltage, both 20 and 30 V_{pp} give a similar maximum aggregation factor, but at 30 V_{pp} the response time is considerably faster. In the next section, a straight waveguide will be implemented as the intermediate stage towards the Mach-Zehnder integration.

3.4 Integrating surface straight waveguide for optical bio-sensing

In the previous section, the DEP and the trapping of the beads were successfully demonstrated. At this part, a straight waveguide is added in order to investigate whether the trapped beads on top of the waveguide absorb or scatter light enough and cause a detectable change in the intensity of light.

3.4.1 Device fabrication

Figure 3.13 depicts the process flow for the creation of the photonic sensor, which includes a Mach-Zehnder interferometer on glass and metallic castellated electrodes surrounding the sensing arm of the Mach-Zehnder. The same process steps can be used if we wanted to fabricate a surface straight waveguide instead.

In order to fabricate the Mach-Zehnder on glass, ion-exchange process is used [51]. The principle lies in the exchange of alkali ions present in the glass (Na^+) with ions of higher polarizability, such as Ag^+, entailing an increase of the refractive index. As already discussed, having a higher refractive index core is essential to guide the light and minimize the losses. The whole process is based on diffusion and thus elevated temperatures are required (350 °C).

In order to transfer the optical function pattern, an appropriate masking layer must be deposited and patterned before the ion-exchange to limit the diffusion of Ag^+ to the apertures of the mask. For this purpose, we initially deposit aluminium on the whole surface of a glass substrate (i) and with standard photolithography processes we etch it at the desired locations.

With the aluminium mask on (ii), the ion-exchange process takes place in order to create the top surface waveguides through the diffusion apertures (iii). After the process is complete, the aluminium is etched leaving us with an integrated Mach-Zehnder embedded on glass (iv).

Finally, by employing once again standard photolithography, the metallic electrodes (with each tooth and the gaps "v_gap", "h_gap" set at 50 μm) are implemented thus giving us the complete device (v-vi).

Like before, a PDMS encapsulation can be also implemented (vii) with a channel height fixed (by laboratory's technology) at 39 μm and with the other dimensions related to the microfluidic design to be used.

3.4.2 Testbench

In figure 3.14 the testbench is presented. With the addition of a straight waveguide or a Mach-Zehnder few other components are added to the configuration described in figure 3.3. A laser source is used to inject light to the fiber coupled to the input of the waveguide. Another fiber, coupled to

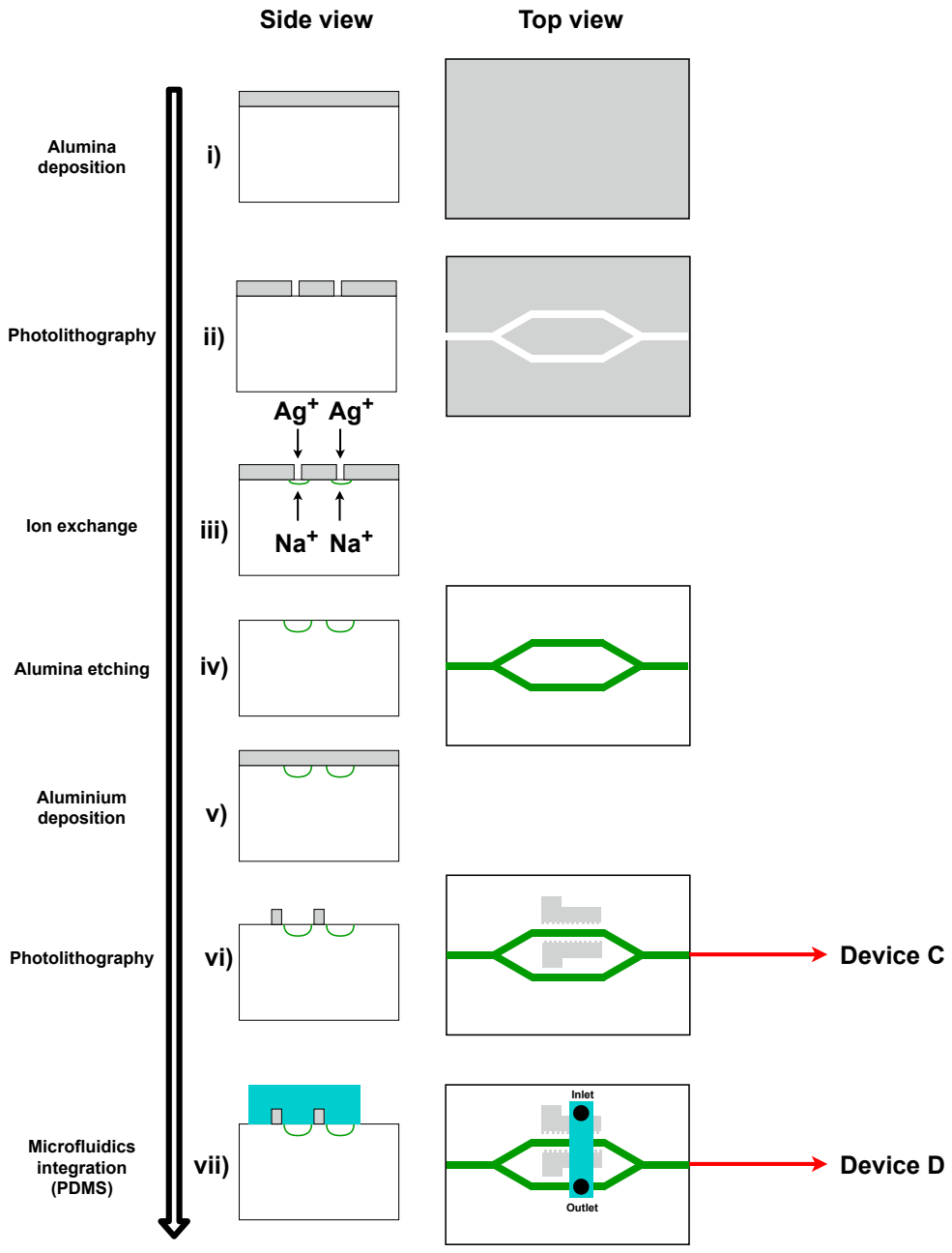

Figure 3.13: Process flow for the development of the integrated, photonic sensor.

the output of the waveguide is connected to a photodetector in order to monitor the intensity of the light. Like before, the sample is observed by means of an optical microscope connected with a computer. The fibers and the waveguides are visible along with the glass, the electrodes and the probes.

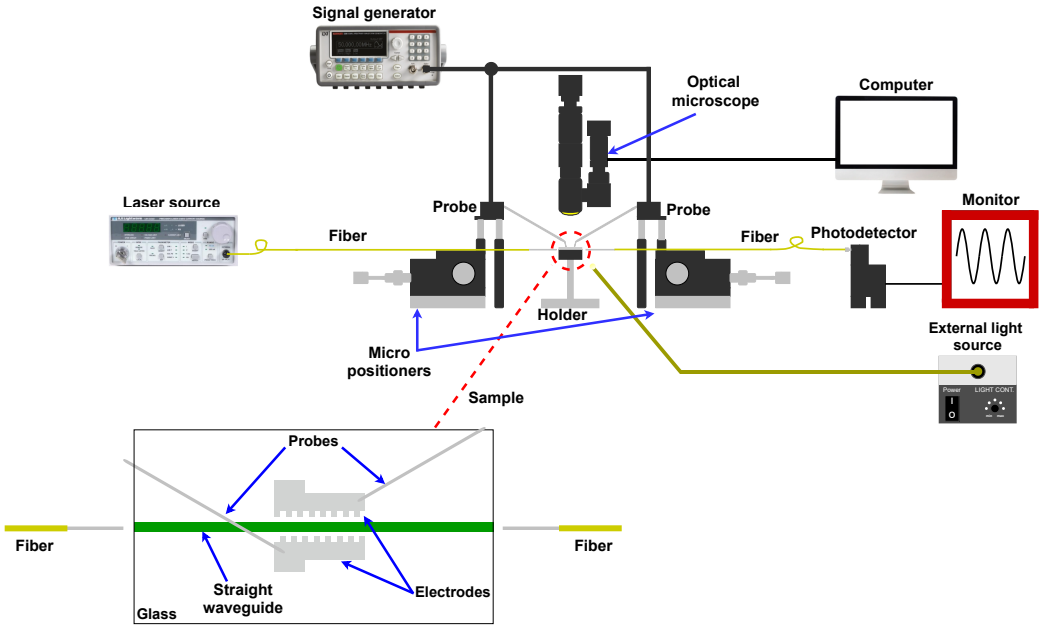

Figure 3.14: The developed testbench for the biasing and the optical characterization of the sensor.

3.4.3 Detection of latex beads based on optical losses

As a first step, light was injected through the waveguide with an output reference intensity equal to $P_{\text{ref}} = 12$ μW. A droplet of 2 μl containing the charged beads was deposited on top of the straight waveguide between the electrodes. Without the application of an AC signal, the system was let to reach a steady state for approximately 6 minutes giving us the transmitted power, P_{off}.

Alternating signals between 100 kHz (2 minutes) and 5 MHz (1 minute) were applied at 20 V_{pp}. The power corresponding to the transmitted power after the application of an AC signal is represented by P_{on}. The results are shown in figure 3.15. The relative difference of the transmitted power, defined as $\frac{\Delta P}{P_{\text{off}}} = \frac{P_{\text{on}} - P_{\text{off}}}{P_{\text{off}}}$ with respect to running time is reported on the vertical axis of the graph. The duration in the x axis is measured from the moment an AC signal was applied. The time needed to reach a steady state prior to the signal is omitted in this graph.

When a 100 kHz signal is applied, a reduction in the optical power is observed. This can be ascribed to either absorption or scattering effects due to the accumulation of the beads on top of the straight waveguide. Instead, when a signal of 100 MHz is applied, the optical power is restored, as the beads are removed from the surface. In both cases, a plateau is reached.

During the experiment a reduction in the peaks' magnitude is observed. As the droplet is drying, trapping is less efficient. From the 3rd cycle and onwards, the change becomes more apparent. Nonetheless, these results clearly demonstrate that the trapping of the beads is sufficient to be detected as a change of around -8% is noted with a response and recovery time in the order of 2 and 1 minute respectively. Therefore, the functionality of the developed optical bio-sensor is verified.

Due to lack of time, we could not test the Mach-Zehnder interferometer function. It will thus be the subject of further investigation.

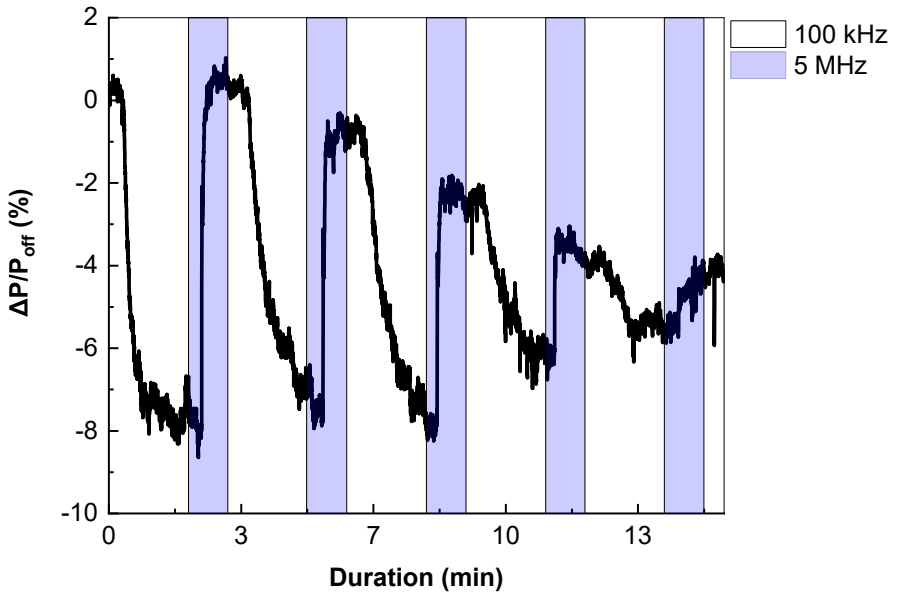

Figure 3.15: The line plot of the relative difference of the transmitted power with respect to time. The measurement consists of five frequency cycles. Each frequency cycle consists of 2 min at 100 kHz alternated with 5 MHz for 1 minute. At 100 kHz we have pDEP and the latex beads aggregate on top of the waveguide leading to absorption and scattering effects of the light. At 5 MHz, they are removed, resetting the signal.

3.5 Conclusion

In this chapter we began by presenting the latex beads. The latex beads of our choice were of two categories, charged and uncharged in order to mimic dead and viable cells respectively. Among the different qualities of water tested, deionized water was chosen for the dilution of the latex beads as its impurities do not hide their presence.

Next, AC electrokinetics experiments took place on a sample consisting of metallic castellated electrodes on glass. After the process flow and the testbench were shown, both kinds of beads were tested with different AC signals. In both charged and uncharged beads nDEP was observed, whereas only for the former pDEP was verified. Finally, a home-made Python script was presented and used for further exploration of the images of trapped beads, acquired with an optical microscope. By making use of the script, the crossover frequency was estimated at around 1.67 MHz which is in agreement with the bibliography. Moreover, it was found that the trapping was more efficient for frequencies between 100 and 200 kHz. On the other hand, concerning the applied voltage, for a value of 20 or 30 V_{pp} the trapping was more effective (with respect to 10 V_{pp}), with the latter also resulting in a significantly faster accumulation as well.

At the final part, a straight surface waveguide was added prior to the integration of the metallic electrodes and AC electrokinetics experiments were repeated by making use of the optimal values for pDEP found in the previous section. We found that the trapped beads are able to absorb or scatter the injected light and cause a relative difference in the transmitted power of approximately -8% for 20 V_{pp} and 100 kHz. With the proper design of the sensing area and the right applied AC signal the amount of optical losses can be tuned. These first results show that it is possible to both sense the beads and pave the way to further studies correlating the optical losses with their concentration.

Chapter 4

Conclusion and Perspectives

In this thesis, we proposed an AC electrokinetics-based integrated photonic sensor to meet the current gap in technology, concerning cost-effective solutions for reliable, robust, real-time biosensing for water monitoring. Towards that goal, we explored the various AC electrokinetics phenomena and we identified that among the parameters that should be tuned to favor dielectrophoresis, frequency plays the most important role. Moreover, by using the COMSOL software we located the areas where the polystyrene latex beads would be trapped under the DEP effect. In addition, we identified that the vertical gap between the electrodes is the most important geometrical parameter to consider when we want to optimize the system. As far as the optical component is concerned, we concluded by using the Lumerical software that for the detection of polystyrene latex beads, the waveguides should have a depth and width equal to 1.25 μm in order to be single-mode. Finally, we saw that in order to not induce a phase difference between the two arms of a Mach-Zehnder interferometer higher than $\frac{\pi}{4}$, the order of magnitude of the interaction length should be 9.44 μm. This is under the strong simplification that the beads constitute an homogeneous layer.

Regarding the experimental processes, we created the testbench that could simultaneously accommodate the tools for both the electrical biasing and fiber characterization. At the same time, the polystyrene latex beads were prepared by diluting them with deionized water and checking their visibility under the optical microscope. Finally, all the different devices used during the experiments were fabricated in the clean room and all the PDMS processes, which include both its development and its bonding with the glass, were fully explored.

During the AC electrokinetics experiments, we tuned the frequency to optimize dielectrophoresis and we managed to control in a reliable and reproducible way the trapping of polystyrene latex beads on a device consisting of castellated metallic electrodes on glass. Towards that goal, a home-made, image analysis Python script was also developed to analyze the trapping of the beads.

Finally, we fabricated a device with an added optical function, which includes a surface straight waveguide or a Mach-Zehnder. Being limited by the time, we mainly investigated integrated optical devices without microfluidic cover, manually depositing droplets by means of a pipette.

The first results were promising: We successfully created an optical bio-sensor that was able to detect the aggregated polystyrene latex beads that were trapped on top of the straight waveguide. A variation of around -8% in the relative difference of the transmitted power was observed with the presence of the beads with response and recovery time in the order of few minutes. These results show that the optical losses can be tuned and controlled in various ways (frequency, beads' concentration, electrodes design etc.) giving us much flexibility and room for further improvement.

To conclude, among the declared objectives in section 1.5, the following were completed:

1. Identify and understand the dynamics of AC electrokinetics ✓
2. Create a testbench that accommodates the tools for both the electrical biasing and fiber characterization ✓
3. Tune both bench and processes to clearly distinguish the particles under study ✓

4. Master the PDMS processes with respect to both creating it and bonding it on glass ✓
5. Study and implement electrodes on glass ✓
6. Trap in a reliable and reproducible manner the particles under study to the desired locations ✓
7. Create a functional optical bio-sensor with the implementation of a straight waveguide. ✓

The last objective, concerning the implementation of the Mach-Zehnder function, was not fully reached due to a lack of time but a first estimation of the interaction length has been calculated.

In the rest of the chapter, we present the perspectives which include some steps that could of interest to be focused next.

4.1 Perspectives

Influence of the microfluidic packaging

At the end of the experimental campaign, we tried to correlate the variation of the signal during the trapping phase to the beads concentration. Since we were running out of time, we decided to use droplets of solution, deposited with a pipette. However, this method makes it difficult to control the interaction length. Attempts were thus made to correlate the interaction length with the size of the deposited droplets. For this purpose, pictures of the system have been taken as shown in figure 4.1. The length was estimated by calibrating the image knowing the size of the electrodes teeth.

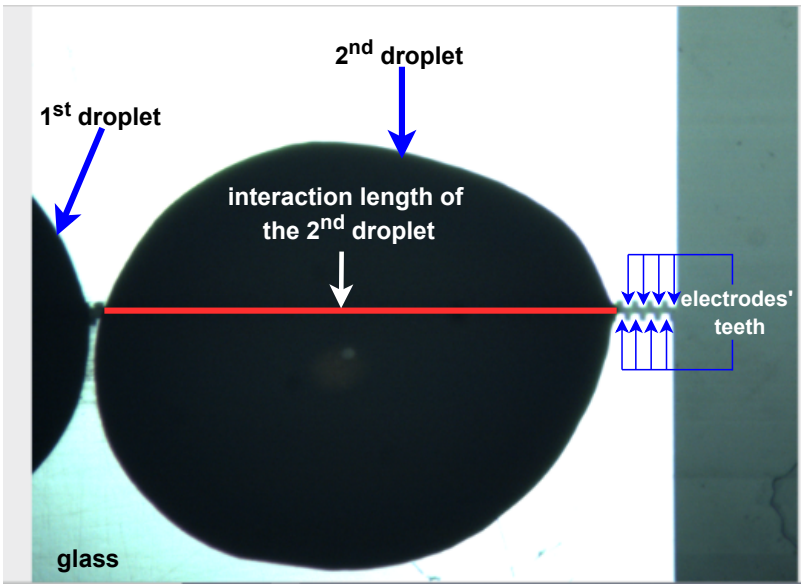

Figure 4.1: Two droplets were deposited on top of the straight waveguide in the middle of the electrodes. The interaction length of the 2nd droplet is shown. Knowing the real dimension of an electrode tooth (50 μm), the interaction length is estimated. For example, by measuring the relative lengths, the red line is found to have a length equal to the sum of the lengths of 35 teeth. Thus, it is calculated: $50 \times 35 = 1750$ μm

We repeated the experiment few times under the same conditions, by changing only the number of droplets with the beads deposited between the electrodes on top of the waveguide. Due to the large size of the droplets, only two of them could be deposited on the electrodes' teeth. In total three experiments were realized:

- Depositing one droplet on the electrodes teeth (repeated two times on different locations)
- Depositing two droplets

In order to calculate the absorption coefficient the following formula was used due to having long propagation length:

$$\alpha = -\frac{1}{L} ln \frac{P_{\text{on}}}{P_{\text{off}}} \tag{4.1}$$

where P_{on} the transmitted optical power after the application of pDEP and the reach of saturation, P_{off} the incident optical power just before applying pDEP and L the length of the electrodes' part which is under the droplet(s).

The results were found:

- $\alpha = 0.00029$ Np/μm for the first experiment of depositing one droplet
- $\alpha = 0.00031$ Np/μm for the second experiment of depositing one droplet
- $\alpha = 0.00055$ Np/μm for the experiment of depositing two droplets

The results concerning one droplet are logical and show that the measurements are repeatable since the variation between both is less than 10%. However, we should get the same order of magnitude for the absorption coefficient extracted from the two droplets measurement since the concentration of beads is the same. We suspect that the shape and the height of the liquid layer is not the same in the case of the two droplets, which influences the interaction between the guided light and the superstrate.

This proves an additional limitation to the droplet-based experiments. When using a droplet to insert the beads, not only we are time-limited due to the drying forces which become dominant over time, but also we are unable to precisely control the length and the height of interaction. Therefore, switching completely to the integration of a microfluidic channel for the insertion of the beads should be the next step. This way the length of interaction will be fixed and the controllability of the system will not be affected as it would have by the drying forces of the droplet.

Tests with packaged microfluidic channels in PDMS

During this project, we were able to successfully trap and control the beads. We were able to fabricate two packaged devices. The first one includes both electrodes for the DEP and a microfluidic channel of PDMS and is shown in figure 4.2 (a). The second one comprises also a straight waveguide between the electrodes gap and is shown in figure 4.2 (b). In both cases a trapping effect was observed. However, the phenomenon is much weaker in the second device. This has been attributed to a smaller size of the second microfluidic channel entailing a greater difficulty to control the flow. The resulting perturbation masks the trapping effect.

Increasing the width of the channel is a simple way to try solve the problem. This however would require a bigger portion of the area to be available for bonding in addition to needing a much more precise handling, as during the bonding we would have to leave adequate space in the electrodes for the biasing probes to land.

A better way to handle this is by increasing the effect of DEP. As discussed in chapter 2 the most effective way to accomplish that is by reducing the gap between the electrodes. That way the dielectrophoretic force will be much stronger and in addition the beads will not have to cover the whole middle region and form the "zig-zag" pattern. The straight waveguide will be significantly closer to the edges of the electrodes where the maximum dielectrophoretic force is observed. This can be seen in (b) as well. If the waveguide was under the already trapped beads, it is plausible that we would be able to have an intensity modulation even without the full capture of the middle region.

Another solution could be to invest on a extremely precise pump that would be able to apply very low pressure and inject little flow with small velocity.

All in all, based on the aforementioned, the following steps are proposed:

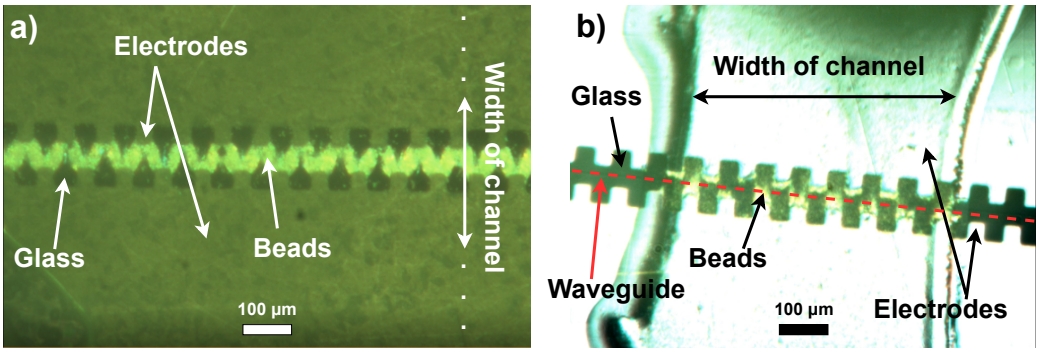

Figure 4.2: Images acquired by an optical microscope depicting pDEP effect inside the PDMS channels. The sample with the beads was injected through a syringe. Besides the PDMS that is present in both, in (a) we have only metallic electrodes on glass, while in (b) we also have a straight waveguide. In both cases pDEP is present, but on the left picture it is more evident and the "zig-zag" pattern can be distinguished. In (a) the channel has a big width that exceeds the dimensions of the picture as opposed to (b).

1. Switch from droplet-based to microfluidic-based measurements to eliminate drying and fix the interaction length and height.
2. Design electrodes with smaller gaps for a stronger DEP effect.
3. By using various PDMS channels of different widths, repeat the experiments to extract the absorption coefficient.
4. By having a fixed PDMS channel, identify the effect of beads' concentration on the optical losses and trace a calibration curve of the sensor.
5. Perform the measurements on the Mach-Zehnder interferometer and confront the results with the interaction length calculated in section 2.4.1.

Bibliography

[1] Wikipedia contributors, "Lubrizol factory fire in rouen — Wikipedia, the free encyclopedia," 2020. [Online; accessed 31-May-2021].

[2] C. Giuliano, C. Patel, and P. Kale-Pradhan, "A guide to bacterial culture identification and results interpretation.," *P & T : a peer-reviewed journal for formulary management*, vol. 44 4, pp. 192–200, 2019.

[3] P. Kruse, "Review on water quality sensors," *Journal of Physics D: Applied Physics*, vol. 51, p. 203002, 05 2018.

[4] S. Gupta, K. Ramesh, S. Ahmed, and V. Kakkar, "Lab-on-chip technology: A review on design trends and future scope in biomedical applications," *International Journal of Bio-Science and Bio-Technology*, vol. 8, pp. 311–322, 10 2016.

[5] A. Rezk, J. Friend, and L. Yeo, "3 - actuation mechanisms for microfluidic biomedical devices," in *Microfluidic Devices for Biomedical Applications* (X. J. Li and Y. Zhou, eds.), Woodhead Publishing Series in Biomaterials, pp. 100–138, Woodhead Publishing, 2013.

[6] S. Ray, G. Mehta, and S. Srivastava, "Label-free detection techniques for protein microarrays: Prospects, merits and challenges," *PROTEOMICS*, vol. 10, no. 4, pp. 731–748, 2010.

[7] G. Seo, G. Lee, M. J. Kim, S.-H. Baek, M. Choi, K. B. Ku, C.-S. Lee, S. Jun, D. Park, H. G. Kim, S.-J. Kim, J.-O. Lee, B. T. Kim, E. C. Park, and S. I. Kim, "Rapid detection of covid-19 causative virus (sars-cov-2) in human nasopharyngeal swab specimens using field-effect transistor-based biosensor," *ACS Nano*, vol. 14, no. 4, pp. 5135–5142, 2020. PMID: 32293168.

[8] A. Ansari and P. Imoukhuede, "Plenty more room on the glass bottom: Surface functionalization and nanobiotechnology for cell isolation," *Nano Research*, vol. 11, 09 2018.

[9] L. Nicu and T. Leïchlé, "Biosensors and tools for surface functionalization from the macro- to the nanoscale: The way forward," *Journal of Applied Physics*, vol. 104, no. 11, p. 111101, 2008.

[10] Q. Chen and Y. J. Yuan, "A review of polystyrene bead manipulation by dielectrophoresis," *RSC Adv.*, vol. 9, pp. 4963–4981, 2019.

[11] L. Hetier, "Conception d'un système de piégeage par diélectrophorèse sur un bras de mesure photonique," Master's thesis, IMEP-LaHC, France - Grenoble, 2020.

[12] J. Liu, *Photonic Devices*. Cambridge University Press, 2005.

[13] B. Chocarro-Ruiz, A. Fernández-Gavela, S. Herranz, and L. M. Lechuga, "Nanophotonic label-free biosensors for environmental monitoring," *Current Opinion in Biotechnology*, vol. 45, pp. 175–183, 2017. Energy biotechnology • Environmental biotechnology.

[14] S. Pathak, "Chapter 7 - photonics integrated circuits," in *Nanoelectronics* (B. K. Kaushik, ed.), Advanced Nanomaterials, pp. 219–270, Elsevier, 2019.

[15] A. Mathesz, S. Valkai, A. Újvárosy, B. Aekbote, O. Sipos, B. Stercz, B. Kocsis, D. Szabó, and A. Dér, "Integrated optical biosensor for rapid detection of bacteria," *Optofluidics, Microfluidics and Nanofluidics*, vol. 2, 01 2015.

[16] D. Sarkar, N. S. K. Gunda, I. Jamal, and S. K. Mitra, "Optical biosensors with an integrated mach-zehnder interferometer for detection of listeria monocytogenes," *Biomedical microdevices*, vol. 16, p. 509—520, August 2014.

[17] Y. Gao, Q. Gan, Z. Xin, X. Cheng, and F. J. Bartoli, "Plasmonic mach–Zehnder interferometer for ultrasensitive on-chip biosensing," *ACS Nano*, vol. 5, no. 12, pp. 9836–9844, 2011. PMID: 22067195.

[18] M. Costella, Q. Avenas, M. Frénéa-Robin, J. Marchalot, P. Bevilacqua, P. G. Charette, and M. Canva, "Dielectrophoretic cell trapping for improved surface plasmon resonance imaging sensing," *ELECTROPHORESIS*, vol. 40, no. 10, pp. 1417–1425, 2019.

[19] N. Tawil, E. Sacher, R. Mandeville, and M. Meunier, "Surface plasmon resonance detection of e. coli and methicillin-resistant s. aureus using bacteriophages," *Biosensors & bioelectronics*, vol. 37, pp. 24–9, 05 2012.

[20] D. Petrovszki, S. Valkai, E. Gora, M. Tanner, A. Bányai, P. Fürjes, and A. Dér, "An integrated electro-optical biosensor system for rapid, low-cost detection of bacteria," *Microelectronic Engineering*, vol. 239-240, p. 111523, 2021.

[21] K. Khoshmanesh, C. Zhang, S. Nahavandi, F. J. Tovar-Lopez, S. Baratchi, A. Mitchell, and K. Kalantar-Zadeh, "Size based separation of microparticles using a dielectrophoretic activated system," *Journal of Applied Physics*, vol. 108, no. 3, p. 034904, 2010.

[22] H. Matbaechi Ettehad, P. Soltani Zarrin, R. Hölzel, and C. Wenger, "Dielectrophoretic immobilization of yeast cells using cmos integrated microfluidics," *Micromachines*, vol. 11, no. 5, 2020.

[23] B. Kirby, *Micro- and Nanoscale Fluid Mechanics: Transport in Microfluidic Devices*. Cambridge University Press, 2010.

[24] M. Punjiya, H. Rezaei Nejad, J. Mathews, M. Levin, and S. Sonkusale, "A flow through device for simultaneous dielectrophoretic cell trapping and ac electroporation," *Scientific Reports*, vol. 9, 08 2019.

[25] M. E. Doyle and K. A. Glass, "Sodium reduction and its effect on food safety, food quality, and human health," *Comprehensive Reviews in Food Science and Food Safety*, vol. 9, no. 1, pp. 44–56, 2010.

[26] W. H. Sperber, "Influence of Water Activity on Foodborne Bacteria — A Review," *Journal of Food Protection*, vol. 46, pp. 142–150, 02 1983.

[27] J. Cottet, O. Fabregue, C. Berger, F. Buret, P. Renaud, and M. Frénéa-Robin, "MyDEP: a new computational tool for dielectric modeling of particles and cells," Jan. 2019.

[28] W. T. Winter and M. E. Welland, "Dielectrophoresis of non-spherical particles," *Journal of Physics D: Applied Physics*, vol. 42, p. 045501, jan 2009.

[29] P. K. Wong, T.-H. Wang, J. Deval, and C.-M. Ho, "Electrokinetics in micro devices for biotechnology applications," *IEEE/ASME Transactions on Mechatronics*, vol. 9, no. 2, pp. 366–376, 2004.

[30] J. Oh, R. Hart, J. Capurro, and H. M. Noh, "Comprehensive analysis of particle motion under non-uniform AC electric fields in a microchannel," *Lab Chip*, vol. 9, pp. 62–78, 2009.

[31] P. García-Sánchez and A. Ramos, *AC Electroosmosis: Basics and Lab-on-a-Chip Applications*, pp. 25–30. Dordrecht: Springer Netherlands, 2012.

[32] N. Green, A. Ramos, A. González, H. Morgan, and A. Castellanos, "Fluid flow induced by non-uniform ac electric fields in electrolytes on microelectrodes iii: Observation of streamlines and numerical simulation," *Physical review. E, Statistical, nonlinear, and soft matter physics*, vol. 66, p. 026305, 09 2002.

[33] N. G. Green, A. Ramos, A. González, H. Morgan, and A. Castellanos, "Fluid flow induced by nonuniform ac electric fields in electrolytes on microelectrodes. i. experimental measurements," *Phys. Rev. E*, vol. 61, pp. 4011–4018, Apr 2000.

[34] P.-K. Wong, T.-H. Wang, J. Deval, and C.-M. Ho, "Electrokinetics in micro devices for biotechnology applications. ieee/asme trans mechatron 9:366-376," *Mechatronics, IEEE/ASME Transactions on*, vol. 9, pp. 366 – 376, 07 2004.

[35] A. Salari, M. Navi, T. Lijnse, and C. Dalton, "Ac electrothermal effect in microfluidics: A review," *Micromachines*, vol. 10, 2019.

[36] Y. Huang and R. Pethig, "Electrode design for negative dielectrophoresis," *Measurement Science and Technology*, vol. 2, pp. 1142–1146, dec 1991.

[37] H. Sadeghian, Y. Hojjat, and M. Soleimani, "Interdigitated electrode design and optimization for dielectrophoresis cell separation actuators," *Journal of Electrostatics*, vol. 86, pp. 41–49, 2017.

[38] C. Iliescu, G. Tresset, L. Yu, and G. Xu, "3D dielectrophoretic chips: Trapping and separation of cell populations," *Romanian Journal of Information Science and Technology*, vol. 13, pp. 49–64, 01 2010.

[39] D. Petrovszki, S. Valkai, E. Gora, M. Tanner, A. Bányai, P. Fürjes, and A. Dér, "An integrated electro-optical biosensor system for rapid, low-cost detection of bacteria," *Microelectronic Engineering*, vol. 239-240, p. 111523, 2021.

[40] N. G. Green, A. Ramos, and H. Morgan, "Ac electrokinetics: a survey of sub-micrometre particle dynamics," *Journal of Physics D: Applied Physics*, vol. 33, pp. 632–641, mar 2000.

[41] A. Dalili, E. Taatizadeh, H. Tahmooressi, N. Tasnim, P. Rellstab-Sánchez, M. Shaunessy, H. Najjaran, and M. Hoorfar, "Parametric study on the geometrical parameters of a lab-on-a-chip platform with tilted planar electrodes for continuous dielectrophoretic manipulation of microparticles," *Scientific Reports*, vol. 10, 07 2020.

[42] D. Yuan, Y. Dong, Y. Liu, and T. Li, "Mach-zehnder interferometer biochemical sensor based on silicon-on-insulator rib waveguide with large cross section," *Sensors*, vol. 15, no. 9, pp. 21500–21517, 2015.

[43] M. Kitsara, K. Misiakos, I. Raptis, and E. Makarona, "Integrated optical frequency-resolved mach-zehnder interferometers for label-free affinity sensing," *Opt. Express*, vol. 18, pp. 8193–8206, Apr 2010.

[44] Hammer, "Simulations in integrated optics - a collection of online resources." `https://www.siio.eu/index.html`.

[45] D. M. Knauss, "Modern styrenic polymers: polystyrenes and styrenic copolymers edited by john scheirs (excelplas australia, edithvale) and duane priddy (priddy & associates, llc, midland, mi). j. wiley and sons, ltd: chichester. 2003. xxxiv + 758 pp. isbn 0-471-49752-5.," *Journal of the American Chemical Society*, vol. 126, no. 14, pp. 4741–4741, 2004.

[46] H. Wang, L. Yang, and G. Rempel, "Homogeneous hydrogenation art of nitrile butadiene rubber: A review," *Polymer Reviews*, vol. 53, 05 2013.

[47] S. Rao Balakrishnan and M. Asri, "Conventional photolithography and process optimization of pattern-size expansion technique for nanogap biosensor fabrication," *Advanced Materials Research*, vol. 832, pp. 89–94, 01 2014.

[48] C. Mack, *Fundamental Principles of Optical Lithography: The Science of Microfabrication*, ch. 1, pp. 1–28. John Wiley & Sons, Ltd, 2007.

[49] M. D. Vahey and J. Voldman, "High-throughput cell and particle characterization using isodielectric separation," *Analytical Chemistry*, vol. 81, no. 7, pp. 2446–2455, 2009. PMID: 19253950.

[50] K. Khoshmanesh, C. Zhang, S. Nahavandi, F. J. Tovar-Lopez, S. Baratchi, A. Mitchell, and K. Kalantar-zadeh, "Size based separation of microparticles using a dielectrophoretic activated system," *Journal of Applied Physics*, vol. 108, no. 3, p. 034904, 2010.

[51] J.-E. Broquin, "Glass integrated optics: state of the art and position toward other technologies," in *Integrated Optics: Devices, Materials, and Technologies XI*, vol. 6475, p. 647507, International Society for Optics and Photonics, 2007.

Abstract

Developing real-time, label-free and portable bio-sensors for water monitoring is crucial for the general well-being. Glass integrated photonics is a promising technology to employ due to its bio-compatibility, robustness and high sensitivity. This project is dedicated to the development of an optical bio-sensor based on a principle of interferometry or on absorption and scattering effects and uses electrokinetic phenomena in alternating current to capture bacteria sensitive to pollution. The compatibility of the electrodes with the glass and the absence of surface functionalization make it a perfectly suitable solution for reliable and low-cost sensors. In this study, the photonic circuit, implemented by silver-sodium ion-exchange on glass, is co-integrated using standard photolithography processes with aluminum electrodes designed to optimize dielectrophoresis. Charged polystyrene latex beads (Aldrich, CLB9) dispersed in deionized water are used to model the bacteria. The sensor is exposed to the sample either through a microfluidic channel made of polydimethylsiloxane (PDMS) or by directly depositing a drop on the sensitive surface. Various alternating current signals are applied on the electrodes and their effects on the capture of the micro-spheres are evaluated. A home-made Python script is also developed for the analysis of the trapping recorded via an optical microscope. We found that a frequency in the range of 50 - 200 kHz is needed to maximize the trapping of the beads with an applied voltage of at least 20 V_{pp}. We also observed a variation in the optical losses of the guided optical signal at a wavelength of 1550 nm by selectively controlling the trapping. The response times of the sensor following alternating trapping and de-trapping of the beads are of the order of minutes with relative signal variations greater than 8% between these two states.

Le développement, pour la mesure de la qualité de l'eau, de biocapteurs temps-réel, portables et sans marqueurs est un point crucial pour le suivi environnemental. La photonique intégrée sur verre est une technologie prometteuse dans ce domaine grâce à sa biocompatibilité, sa robustesse et sa grande sensibilité. Ce projet implique la fabrication d'un biocapteur optique basé sur un principe d'interférométrie ou d'absorption et emploie des effets électrocinétiques en courant alternatif (diélectrophorèse) pour piéger des bactéries sensibles à la pollution. La compatibilité des électrodes avec le verre ainsi que l'absence de couche de fonctionnalisation en font une solution parfaitement adaptée pour une détection fiable et à bas-coût. Dans cette étude, le circuit optique, inscrit dans le substrat de verre par un échange d'ions Ag+/Na+, est co-intégré grâce à des procédés standards de photolithographie aux électrodes d'aluminium conçues pour optimiser les phénomènes de diélectrophorèse (DEP). Des billes de polystyrène latex chargées (Aldrich, CLB9) dispersées dans de l'eau désionisées sont utilisées pour modéliser les bactéries cibles. La solution est introduite au niveau du capteur soit par un circuit microfluidique en polydimethylsiloxane (PDMS) soit en déposant directement une goutte à la surface de la zone sensible. Différents signaux électriques alternatifs sont appliqués aux électrodes et leurs effets sur le piégeage des billes sont évalués. Un script python a également été développé pour évaluer l'efficacité du piégeage à partir d'images acquises par microscopie optique. Nous avons déterminé qu'une fréquence comprise entre 50 et 200 kHz et une tension appliquée de 20 Vpp sont nécessaires pour optimiser le piégeage des billes au voisinage du circuit optique. Nous avons également observé une variation de l'absorption du signal optique guidé à la longueur d'ondes de 1550 nm en contrôlant sélectivement le piégeage. Les temps de réponse du capteur suite à des alternances de piégeage et dé-piégeage des billes sont de l'ordre de quelques minutes avec des variations relatives de signal supérieures à 8% entre ces deux états.

Lo sviluppo di bio-sensori funzionanti in tempo reale, portatili e senza traccianti chimici è un punto cruciale per la sorveglianza dell'ambiente. La fotonica integrata su vetro è una tecnologia promettente in questo campo, per la sua bio-compatibilità, la sua robustezza e la sua grande sensibilità. Questo progetto è dedicato alla fabbricazione di un bio-sensore ottico basato su un principio di interferometria o di assorbimento ed utilizza effetti elettrocinetici in corrente alternata (dielettroforesi) per catturare dei batteri sensibili all'inquinamento. La compatibilità degli elettrodi con il vetro e l'assenza di una funzionalizzazione superficiale la rendono una soluzione perfettamente adeguata per sensori affidabili ed a basso costo. In questo studio, il circuito ottico, fabbricato in un substrato di vetro con uno scambio ionico Ag+/Na+ è co-integrato tramite processi standard di fotolitografia con elettrodi di alluminio progettati per ottimizzare i fenomeni di dielettroforesi (DEP). Un lattice di micro-sfere di polistirene cariche (Aldrich, CLB9) disperse in acqua deionizzata è utilizzato per modellizzare i batteri. La dispersione è introdotta nel sensore o tramite un circuito microfluidico in polidimetilsilossano (PDMS), oppure depositando direttamente una goccia sulla superficie sensibile. Diversi segnali elettrici in corrente alternata sono applicati agli elettrodi ed i loro effetti sulla cattura delle micro-sfere sono valutati. Uno script Python è stato inoltre sviluppato per valutare l'efficienza di cattura, partendo da immagini ottenute per microscopia ottica. Si è ottenuto che una frequenza compresa tra 50 e 200 kHz ed una tensione applicata di 20 Vpp sono necessarie per ottenere una cattura delle micro-sfere in prossimità del circuito ottico. Una variazione dell'assorbimento in guida d'onda del segnale ottico alla lunghezza d'onda di 1550 nm è stata osservata controllando la cattura in maniera selettiva. Il tempo di risposta del sistema in seguito alle alternanze di cattura e rilascio delle biglie è dell'ordine di qualche minuto, con delle variazioni relative di intensità del segnale ottico di oltre 8% fra i due stati.